Scalar Top Searches in Photon-Photon Collisions at TESLA

Hassan Chagani

THE UNIVERSITY
of MANCHESTER

Particle Physics Group

Department of Physics & Astronomy

May 2005

A dissertation submitted to the University of Manchester for the degree of Master of Science in the Faculty of Science and Engineering

Contents

List of Figures

List of Tables

Abstract

The discovery potential of scalar top quarks of mass 180 GeV at the TESLA photon collider is investigated. The neutralino is assigned a mass of 100 GeV, thus giving the decay chain $\tilde{t}_1 \rightarrow c\tilde{\chi}_1^0$ a 100% branching ratio. Rapidities and transverse momenta for stop squark events are generated with a leading order cross-section program. These are converted to momentum-energy vectors and fed into the Monte Carlo event generator PYTHIA. Top-antitop background events are also generated by the same process. The photon-energy spectrum for other background processes is generated using the CompAZ parameterisation. The decay records from PYTHIA are conveyed to the TESLA detector simulation program Simdet. The ZVTOP algorithm, together with a neural network trained on high-energy events, was used to tag charm jets and supply further vertexing information. A series of cuts was performed on the data to primarily remove the main background of W^+W^- events. Distributions for the invariant mass and energy are shown after cuts, and the signal has a significance of about 10 σ. An error on the mass of ± 2 GeV is found.

Declaration

No portion of the work referred to in this dissertation has been submitted in support of an application for another degree or qualification of this or any other university or other institute of learning.

The Author

The author was educated at Latymer Upper School, London, before obtaining a second class B.Sc. (Hons) degree in Physics with Astrophysics at the University of Leeds in 2003. The author joined the Department of Physics & Astronomy at the University of Manchester to read for the degree of M.Sc. in Experimental Particle Physics. The author goes on to study for the degree of Doctor of Philosophy at the University of Sheffield. The work presented in this dissertation was undertaken at the University of Manchester.

Acknowledgements

I would like to thank my supervisor Stefan Söldner-Rembold for his guidance, encouragement and patience over the last year. Without his help and support this work would not have been possible. I would also like to thank Andres Osario for his expert guidance which has improved the programs used to complete this work. Thanks also to Simon Dean for the interesting discussions I had with him late at night on matters that were unrelated to physics.

My thanks to Michael Klasen of Université Grenoble for the kind permission to use his cross-section program, and his patient responses to my questions. He has also been the source of most of the modifications required to the original program over the last year. I would also like to thank Alex Finch of Lancaster University for taking the time to see me in person and explain the research done into scalar top production from electron-positron collisions at TESLA. My thanks also go to Aleksander Filip Żarnecki of Warsaw University who, in absence of a manual, has helped me to create a program which utilises the CompAZ routine. I would like to thank Thorsten Kuhl of DESY, Hamburg for his help with the implementation of the ZVTOP vertex algorithm.

I would like to thank the members of the Particle Physics Group at the University of Manchester for making the last year enjoyable and welcoming a new member to the group.

Special thanks to Nicole Oppler for proof-reading this dissertation, even though she understood none of its content.

Finally, I would like to reserve a special thank you to my mother for her constant and unfailing support during my life, for which I am, and always will be, eternally grateful.

Chapter 1

Introduction

The Standard Model (SM) of particle physics has been resoundingly successful in explaining the observations made in modern day particle physics experiments. However, the validity of this model has been brought into question by recent experimental results and it is plagued by some theoretical problems.

The most popular solution is that given by the theory of Supersymmetry (SUSY), which is simply an extension of the Standard Model. The theory requires the existence of new, and as yet un-detected, particles. Searches for these particles have been conducted at particle accelerators, and lower mass limits have been determined. The results indicate that superparticles tend to be more massive compared with their Standard Model partners.

One of these sparticles is the stop squark $\tilde{t}_1$, which is the supersymmetric partner of the top quark. The lighter mass eigenstate of the stop squark is likely to be the lightest scalar quark, and as a result is a particularly interesting particle.

The next generation linear collider will provide a clean environment in which the properties of stop squarks can be accurately measured. The TeV-Energy Superconducting Linear Accelerator (TESLA) is one of the possible designs. Work has already been undertaken to assess the discovery potential of scalar top quarks from electron-positron collisions at this machine. However, little work has been done into the prospects of stop pair-production in photon-photon interactions. Comparisons between the results in this dissertation and those for electron-positron interactions

will indicate the best way to see the scalar top.

Scalar top pair-production in the context of the Minimal Supersymmetric Standard Model (MSSM) is investigated in this dissertation. Stop squarks of mass 180 GeV are generated by simulating the collisions of Compton-backscattered photon beams which will be produced at a future photon collider. SUSY parameters are adjusted to ensure that the decay channel $\tilde{t}_1 \rightarrow c\tilde{\chi}_1^0$, where c is a charm quark and $\tilde{\chi}_1^0$ is the lightest neutralino, is dominant. Therefore, two c-jets will form part of the signature in the detector for this process.

In the MSSM, the neutralino is the Lightest Supersymmetric Particle (LSP), and has been assigned a mass of 100 GeV for the purposes of this investigation. In the constrained version of the model the LSP is assumed to be stable and weakly interacting. Therefore, a large missing energy is also expected to form part of the signature.

Standard Model background processes, such as quark-antiquark pair-production, are also simulated. The Monte Carlo generator PYTHIA is used to decay signal and background events, and the results are passed through the fast TESLA detector program Simdet. The output from Simdet is passed through a neural network and probabilities for the presence of c-quarks in events are assigned.

A series of cuts are applied to the data in an effort to maximise the signal-to-background ratio. The discovery potential of the scalar top and the errors on its mass are also assessed.

Chapter 2

The TeV-Energy Superconducting Linear Accelerator

2.1 The TESLA Accelerator

Over the past decade there has been a growing consensus among the particle physics community that there is the need for a new linear accelerator for electron-positron collisions. This new accelerator will surpass the collision energies which were available at the Large Electron-Positron (LEP) collider at the European Laboratory for Particle Physics (CERN), Geneva, Switzerland. It will also complement the work being done at the Large Hadron Collider (LHC) at CERN, which is due to start running in 2007.

The TeV-Energy Superconducting Linear Accelerator (TESLA) [1] is one of four possible designs for the next generation linear collider. If chosen, one possible site is at the Deutsches Elektronen-Synchrotron (DESY) research facility in Hamburg, Germany. The TESLA proposal consists of a 33 km linear accelerator stretching from Hamburg to Westhorn, Northern Germany. The tunnels that will contain the body of the accelerator will be at a depth of 10-30 metres, and collisions will take place at a new research facility at Ellerhoop.

The proposed layout of the TESLA accelerator is shown in figure 2.1. A polarised

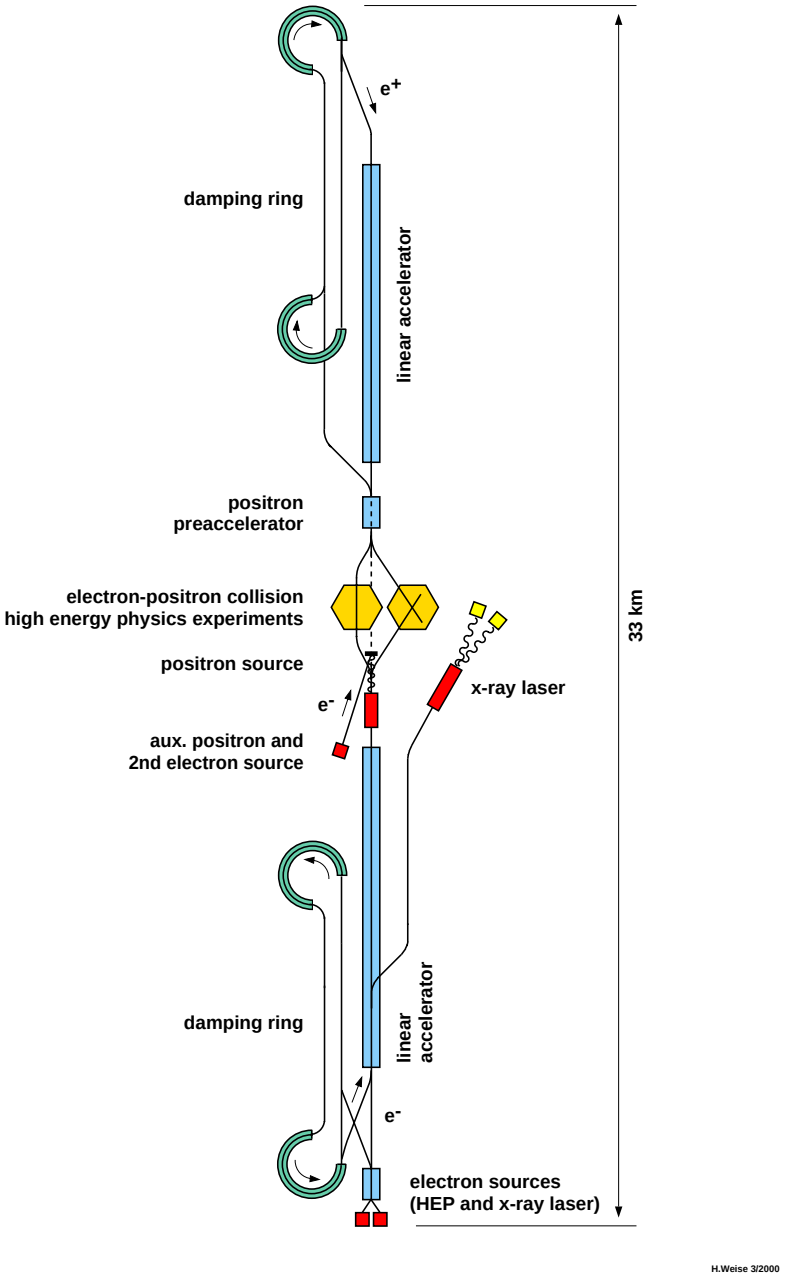

Figure 2.1: Proposed Layout of the TESLA Accelerator. Taken from the TESLA Technical Design Report [1].

laser-driven gun at the research site in Hamburg will be used to generate electrons, which will be passed through a short section of a conventional normal conducting linear accelerator. Here, they will be accelerated to 500 MeV energies, and the beam will then pass through a small section of a superconducting linear accelerator. The superconducting structures used in this section are identical to those in the

main accelerator, and will accelerate the electron beam to 5 GeV. Following this, the electron beam will be transferred to a damping ring to reduce the beam size, a necessity for the high luminosity requirements. Luminosity is a measure of the intensity of a particle beam before interaction with another particle beam or a fixed target. The greater this value the higher the number of collisions when the beam reaches its target. The beam will be compressed and stored in bunches until they are of suitable quality to be decompressed and injected into the main accelerator.

Although there were plans to use those electrons which had survived the collision at the interaction point to generate positrons, they were rejected in favour of a new approach. A different set of electrons will be generated just south of the interaction point and are to be passed through an undulator magnet situated after the main linear accelerator. This will create an intense photon beam, which will be directed towards a titanium-alloy target of thickness 0.4 radiation lengths X_0[†]. This will result in the production of electron-positron pairs, from which the positrons will be extracted and accelerated to 250 MeV in a normal conducting linear accelerator. The positron beam will then be transferred to a superconducting accelerator just north of the interaction point. Here the beam will be accelerated to 5 GeV and then injected into the positron damping ring, where it will be treated in a similar way to the electron beam described previously.

The superconducting cavities in the main accelerator will accelerate the electron and positron beams to 250 GeV, resulting in collisions of 500 GeV centre-of-mass energy. In addition, there is potential for an upgrade to 800 GeV centre-of-mass energy. However, to reach higher collision energies, the main accelerator will need to be extended.

Other possible designs for an electron-positron linear collider include the Next Linear Collider (NLC) [2] at the Stanford Linear Accelerator Centre (SLAC) and the Global Linear Collider (GLC) [3] in Japan. These accelerators comprise of normal conducting materials, unlike the superconducting niobium cavities at TESLA. Less electrical power will be required by the superconducting cavities at TESLA

[†] An electron passing through a material of thickness 1 X_0 will loose energy by a factor of $\frac{1}{e}$.

to accelerate the beams. The low frequency required by the radio frequency (RF) cavities in the main linear accelerator will keep the beam size small. Together, these two factors will allow for high luminosity collisions, which are an essential ingredient at the next linear collider. The Compact Linear Collider (CLIC) [4] at CERN, unlike the designs above, uses technology that needs further research. Recently, a decision has been taken to use superconducting technology at the next generation linear collider [5].

2.2 Photon-Photon Interactions

Photon-photon interactions have been investigated at electron-positron colliders in the past. However, unlike previous electron-positron accelerators, the next generation linear collider will be specifically designed to look at these collisions. The TESLA design has a second interaction point, which will enable photon-photon and electron-positron interactions to occur simultaneously.

2.2.1 Photon Production

Bremsstrahlung and beamstrahlung radiation losses from electron and positron particles and beams have been the source of photon-photon interactions at past particle accelerators. In addition, the photon collider at TESLA [6] will use the principle of Compton-backscattering, which essentially converts an electron beam into a photon beam.

When a charged particle, such as an electron, undergoes acceleration, it can emit radiation in the form of photonic emission. This is known as bremsstrahlung radiation and is inversely proportional to the square of the charged particle's mass. Due to the light mass of the electrons, radiation losses by bremsstrahlung are considerable.

The interaction of a beam of charged particles with the electromagnetic field of the opposing beam results in radiation losses. This process is known as beamstrahlung and is well understood in electron-positron interactions [7].

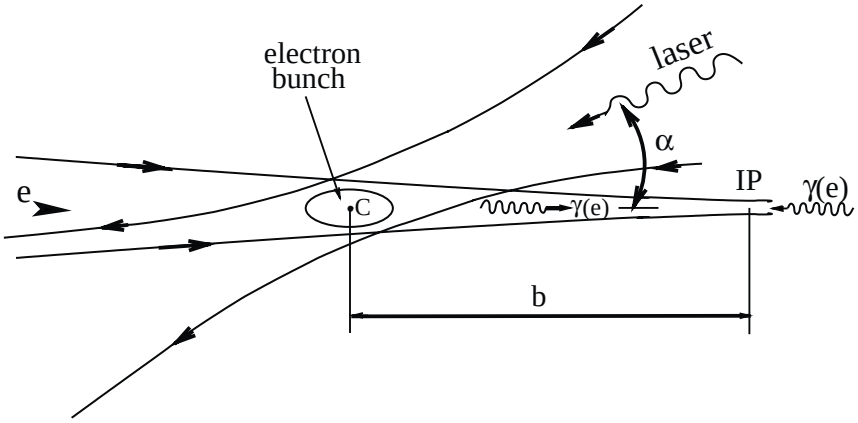

Figure 2.2: Electron to Photon Beam Conversion using the principle of Compton Backscattering at TESLA. Taken from [8].

By making use of Compton backscattering, an electron beam can be converted into a beam of photons, as illustrated in figure 2.2. An electron beam is created and directed into the main accelerator in the same way as described in section 2.1. At a distance b of 1-5 mm from the interaction point IP, the electrons e collide with a focused laser beam at point C. The resultant scattered photons $\gamma(e)$ can have a range of energies, and most will be close to that of the initial electrons. The photons will follow the direction of the initial electron beam towards the interaction point where they will collide with a beam of photons travelling in the opposite direction.

The distance b, between the points C and IP, will need to be large enough to allow electron to photon conversion before the two colliding electron beams can repel each other. The minimum distance to prevent this is approximately 1 mm. In addition, the size of the photon beam must have equal contributions from the electron beam size and the angular spread from Compton scattering, restricting the maximum value of b to approximately 5 mm.

The maximum energy of a scattered photon ω_m depends on the electron beam energy E_0, the energy of the laser beam ω_0, the angle between the laser beam and the resultant photon beam α, and the mass of the electron m_e. It is useful to define a dimensionless quality x such that [9]:

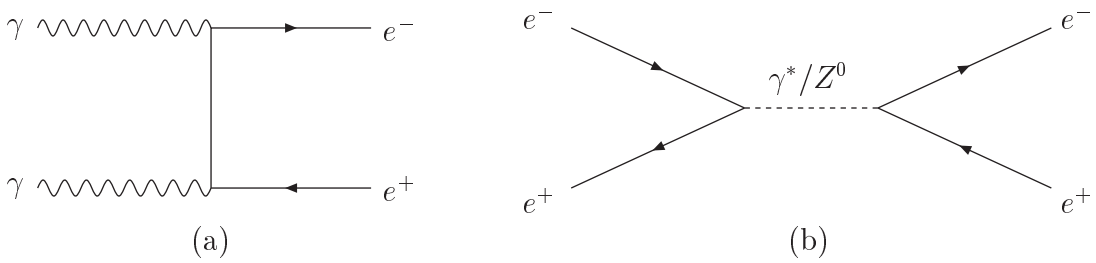

Figure 2.3: Feynman Diagrams for Electron-Positron Pair-Production in: (a) Photon-Photon Interactions and (b) Electron-Positron Interactions.

$$\omega_m = \frac{x}{x+1}E_0\,, \quad x = \frac{4E_0\omega_0}{m_e^2c^4}cos^2\frac{\alpha}{2} \approx 15.3\left[\frac{E_0}{\mathrm{TeV}}\right]\left[\frac{\omega_0}{\mathrm{eV}}\right] = 19\left[\frac{E_0}{\mathrm{TeV}}\right]\left[\frac{\lambda}{\mu m}\right] \quad (2.1)$$

where c is the speed of light and λ is the wavelength of the laser. The collision angle α is assumed to be very small. As an example, if a neodinium glass laser ($\lambda = 1.06\,\mu$m) is used to convert an electron beam of energy 250 GeV, $x = 5$. This results in a maximum photon beam energy of $\omega_m = 0.83E_0 = 209\,\mathrm{GeV}$.

A higher value for x is required to increase the maximum energy of a beam of photons. However, for $x > 4.8$, the produced photons create electron-positron pairs when they collide with the photons in the laser beam [10], effectively reducing the luminosity of photon-photon interactions. With this in mind, the maximum photon beam energy achievable at this value of x is $\omega_m = 0.82E_0 = 206\,\mathrm{GeV}$. This results in a maximum centre-of-mass energy for photon-photon interactions at TESLA of $2\omega_m = 412\,\mathrm{GeV}$.

2.2.2 Comparison with Electron-Positron Interactions

Although photon-photon interactions result in lower centre-of-mass energies than available in electron-positron collisions, they have some distinct advantages.

The cross-sections for charged particle pair-production are higher in photon-photon collisions. The cross-section for a process is a measure of the probability of that interaction occuring. This is mainly due to the lack of an exchange particle

in the production of charged particles from two-photon interactions. Particles are produced in electron-positron interactions by the exchange of a virtual photon γ^* or a Z^0 boson. This is illustrated in figure 2.3.

Unfortunately, Compton backscattering does not result in a pure photon beam. The beam is a mixture of electrons and photons, which leads to electron-electron, electron-photon and photon-photon collisions at the interaction point. This causes a reduction in luminosity at the TESLA photon collider by a factor of three compared with the electron-positron collider.

In addition, the electromagnetic interactions between these particles can cause beamstrahlung photon generation and electron-positron pair-production. These are major sources of backgrounds at a photon collider, but can be reduced by using the crab-crossing scheme [11]. However, the same principle cannot be applied to electron-positron interactions, which also suffer from these backgrounds. Therefore, photon-photon collisions tend to be cleaner than electron-positron interactions.

There is also no need for a positron beam in two-photon collisions. This can be achieved by generating electrons at the second electron source in figure 2.1 without passing the beam through the magnet and titanium-alloy. As positrons are anti-matter particles, their contact with any matter will result in annihilation. Therefore, generating the required charge of 5×10^{13} positrons per beam pulse is a long process, and is not required in two-photon interactions.

The differences between photon-photon and electron-positron interactions are summarised in table 2.1.

2.2.3 Charged Particle Production Cross-Sections

The cross-sections for charged particle production in photon-photon interactions are dependent on several factors. The photon production process, outlined in section 2.2.1, can affect production cross-sections in three ways.

Low-energy photons are created at larger scattering angles, resulting in a bigger photon beam spot size. The density of photons within these beams are lower com-

		Photon-Photon $\gamma\gamma$	Electron-Positron e^+e^-
Centre-of-Mass Energy	E_{CMS} [GeV]	412*	500
Luminosity	L [$10^{34}\,\mathrm{cm}^{-2}\mathrm{s}^{-1}$]	1.1	3.4
Integrated Luminosity	$\mathscr{L}$ [fb^{-1}]	110†	340
Cross-Section for e^+e^- Pair-Production	σ [fb]	6700‡	1070
Events per Year	N_{events} [10^3]	737	364

*Maximum centre-of-mass energy

†Maximum integrated luminosity

‡Cross-section at photon centre-of-mass energies where $\mathscr{L} = 110\,\mathrm{fb}^{-1}$

Table 2.1: Summary of the Comparisons between Photon-Photon and Electron-Positron Interactions. Luminosities taken from the TESLA Technical Design Report [1, 6]. Integrated luminosity calculated for one year of running. Cross-Sections calculated by the event generator PYTHIA 6.222 [13] and the CompAZ [14] routine.

pared with those of higher energy, leading to a suppression of low-energy photon interactions.

With a high-density laser beam, most of the initial electrons will be converted into photons. However, some electrons will still remain, which will have lost little energy before they are rescattered. These particles will contribute to the photon-energy spectrum. In comparison with simple Compton scattering off primary leptons, secondary electrons have a softer energy spectrum.

In addition, if the density of the laser beam is sufficiently high, an electron can scatter off two laser photons. This enhances the high-energy peak of the spectrum.

2.2.4 Photon Polarisation

Varying the linear polarisation of the high energy photons is a useful process which has a number of benefits. It can be used to increase the luminosity of photon-photon interactions and suppress or enhance particle production cross-sections. Linear pho-

ton polarisation can be implemented by polarising the initial electron beam and the laser photons [12].

As a positron beam is not required to produce Compton-backscattered photons, the polarisation of the electron beam will be discussed here. There will be three electron sources for the initial beam. One of these will be a polarised source, which will produce electrons by directing a circularly polarised laser towards a gallium arsenide (GaAs) cathode of surface area 3 cm^2. The laser will be of wavelength 840 nm. The internal components of the gun will need to be kept within an ultra-high vacuum below 10^{-11} mbar. This will maintain a quantum efficiency of 0.1%, which will allow for the high degree of polarisation required (80%). Although a higher degree of electron polarisation would be desirable, this is not possible with the current technology available.

The electrons from this polarised source are injected into a normal conducting linear accelerator to focus the beam. The polarised electrons are then passed through a short section of superconducting linear accelerator before being sent to the damping rings as described in section 2.1.

Photon polarisation can be inverted by changing the sign of electron beam and laser photon polarisations. The luminosity for photon-photon interactions given in table 2.1 assumes that all photons are created from laser photons with 100% circular polarisation and electron beams with 85% longitudinal polarisation. This value will be used throughout this dissertation. Unpolarised photon beams are a mixture of different polarisations.

2.3 The TESLA Detector

The detector at TESLA will be a multipurpose apparatus which needs to achieve the goals set out in the Physics Program [16], meaning that the detector will need to surpass the requirements for the LEP detector. For example, excellent fundamental particle identification and good luminosity evaluation is required for a detector at the next generation linear collider. There are many different possiblities for the

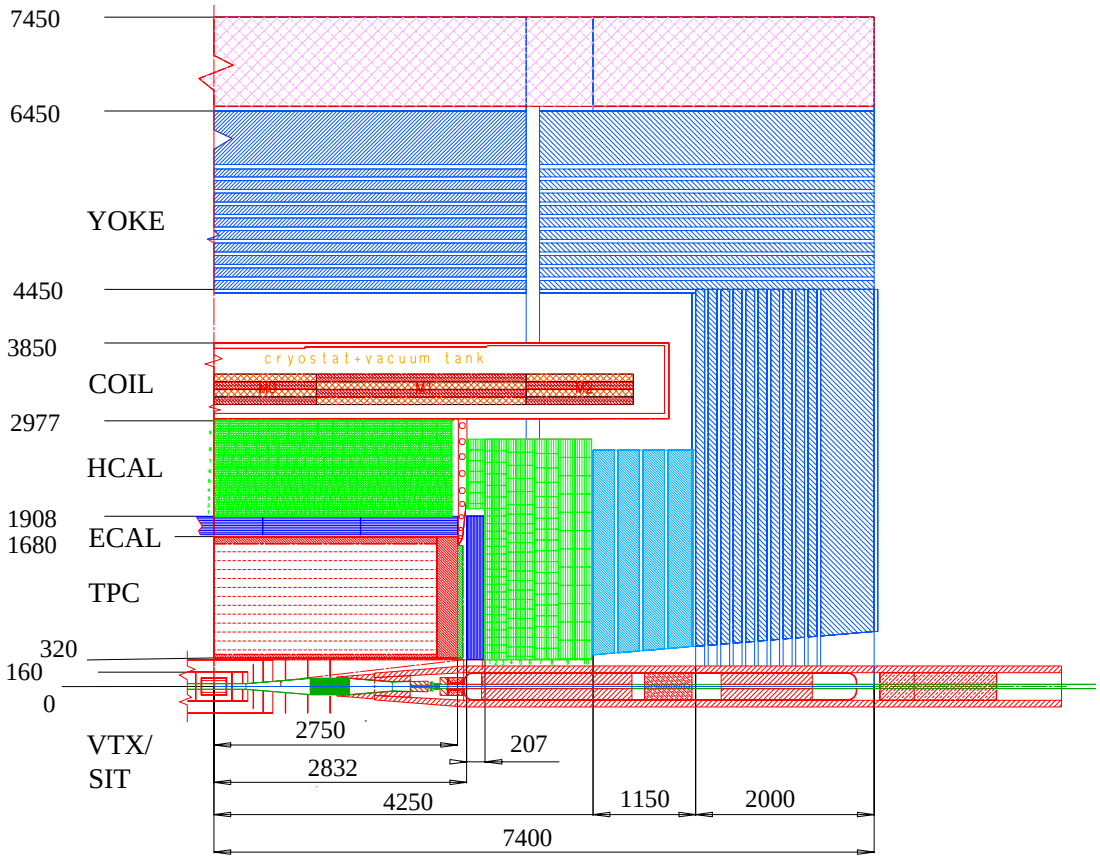

Figure 2.4: Cross-Section of One Quadrant of the Detector at TESLA taken from the TESLA Technical Design Report [15]. Distances are in mm.

design of the detector that will satisfy these criteria, and these will be summarised here.

A barrel-shaped design has been agreed on, of approximate radius 7.5 m and length 15 m, as illustrated in figure 2.4. A system of tracking chambers (VTX, SIT and TPC) and the electromagnetic (ECAL) and hadronic (HCAL) calorimeters are surrounded by a large volume coil (COIL) providing a uniform magnetic field of 4 T. An iron yoke (YOKE) is located outside the coil to ensure that the magnetic field is of the highest quality, and is surrounded by a 1 m deep muon chamber at a radius of 6.45 m from the centre of the detector. The yoke also serves as a muon tracker. A detailed description of the TESLA detector can be found in [15].

In addition, a tungsten mask system will be installed in an attempt to reduce the bremsstrahlung and beamstrahlung backgrounds discussed in section 2.2.2. The

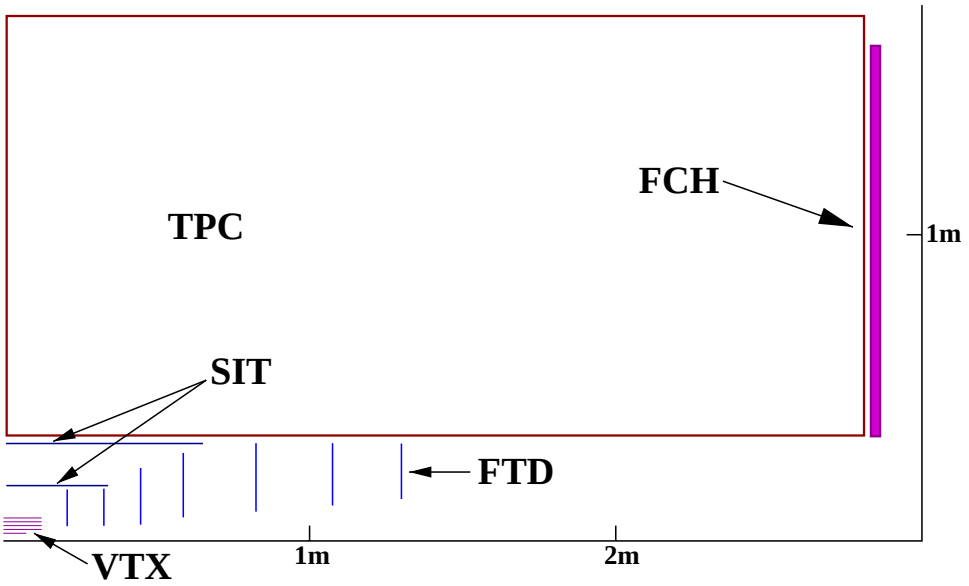

Figure 2.5: Layout of Tracking System at TESLA. Taken from the TESLA Technical Design Report [15].

detector at the Photon Collider, at the second interaction point, will be similar to that for electron-positron interactions. However, there is a system of optics that needs to be contained within the detector.

The coordinate system at TESLA is based on a right-handed Cartesian system, with the origin located at the interaction point. The z-axis is in the direction of the electron beam and the y-axis points upwards. In spherical coordinates, the polar angle θ is defined with respect to the z-axis and the azimuthal angle ϕ with respect to the x-axis. The transverse distance from the z-axis is represented by r.

2.3.1 The Tracking System

The tracking system can be used to determine the sign of charge for charged particles. This is done by encapsulating the tracking system within a magnetic field, causing a charged particle to change its direction of motion dependent on its charge. As a charged particle passes through the detectors, it will ionise the surrounding material creating tracks. Information on the positions of these tracks will be recorded through the collection of released electron pairs, and the curvature of the track can be used to measure the momentum of the particle. Neutral particles do not interact with the

material in the tracking system, so they will not produce tracks. However, they will produce displaced vertices between tracks. Particles which decay within the system can be identified using information from the tracks made by their decay products. A minimal amount of material will be contained within the detectors to optimise these measurements. The detectors will also need to be radiation hard to ensure that they are not damaged by the constant flux of particles passing through them.

The tracking system at TESLA will include a multi-layered pixel micro-vertex detector (VTX), a silicon tracking detector (SIT), and a time projection chamber (TPC). There will be additional silicon discs (FTD) and a forward chamber (FCH) perpendicular to the beam pipe. As mentioned previously, the tracking system will be immersed in a uniform magnetic field of 4 T. The layout of the tracking system is illustrated in figure 2.5. Together, these tracking detectors will reach a high momentum resolution of $5 \times 10^{-5}\,(\mathrm{GeV})^{-1}$.

Micro-Vertex Detector

The vertex detector will be positioned at a radius between 1.5 cm and 6 cm from the interaction point. It will be a high resolution 40 cm long cylindrical structure divided into layers, and its primary function will be to reconstruct secondary vertices in heavy quark (a fundamental particle) flavour decays. Backgrounds from electron-positron pairs will not affect the vertex detector if they are of the order 0.03 hits per mm^2. There are currently four possible design options being considered for the vertex detector: Charge-Coupled Devices (CCDs); Complementary Metal Oxide Semiconductor (CMOS) pixels; Depleted Field Effect Transistor pixels (DEPFET); and Hybrid Active Pixel Sensors (HAPS).

The layouts for the CCD, CMOS and DEPFET options are similar. They will all need a charge collection region of 10 to 20 μm on square-shaped pixels of approximate area 400 $\mu\mathrm{m}^2$. This will enable precision measurements of 1.5 to 3 μm, satisfying the high resolution requirement. They will also provide an angular coverage of $|\cos\theta| < 0.9$.

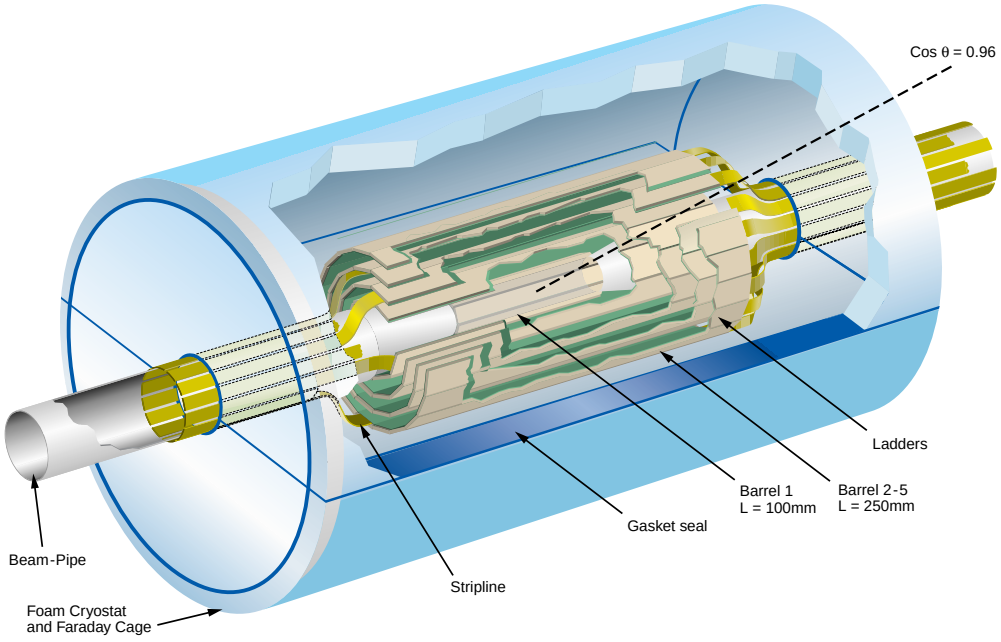

Figure 2.6: Proposed Layout of CCD-Based Micro-Vertex Detector at TESLA. Taken from the TESLA Technical Design Report [15].

Five layers of silicon of thickness 0.06% X_0 at spacings of approximately 11 mm will be contained within the volume of the CCD detector. This arrangement will lead to very high resolutions, enabling very precise tracking for low momenta particles. The layer closest to the beam pipe will be the most susceptible to bremsstrahlung and beamstrahlung background radiation and has a fast readout time of 50 μs to make up for this. The signal charge will be recorded on a row-by-row basis by shifting the signals down the layers using driver chips contained within ladders. These ladders also contain readout chips which receive the analogue signals and converts them to digital output for data storage. Although this design will minimise the material within the detector, it will require a constant, rapid and efficient transfer of signal charge to implement. The proposed layout of the CCD-based vertex detector is shown in figure 2.6.

Similar principles are used in the CMOS design scheme, which is a relatively new proposal. However, signal charges are extracted where they are collected by diffusion in an epitaxial layer. Although this would optimise the performance, further research

is needed to realise the full potential of this method.

The DEPFET design is similar to the CMOS proposal as it will collect signals where they occur. However, the negatively charged signals collected will be cleared and stored by a neighbouring positively charged contact. This sideways depletion action is similar to the use of an epitaxial layer in the CMOS design, and has the same advantages and disadvantages.

Unlike the above designs, the HAPS option will have three detector layers. Active pixel sensors have been used in previous particle physics experiments, and will be used at the Large Hadron Collider (LHC). This means that they are radiation hard and have fast readout capabilities. However, conventional hybrid pixel detectors will not achieve the required minimal spatial resolution of 5 μm, meaning that a new design needs to be implemented. In addition, thicker layers are required by hybrid pixel detectors, increasing the material within the vertex tracker.

Silicon Intermediate Tracker

Lying in between the Vertex Detector (VTX) and the Time Projection Chamber (TPC), the intermediate tracking system will be responsible for improvements in particle momentum measurements and linking tracks found in the TPC and VTX. The Silicon Intermediate Tracker (SIT) will be a part of this system and be composed of two cylinders at a radius of 16 cm and 30 cm from the interaction point, illustrated in figure 2.5. The cylinders will comprise of double sided silicon strip detectors and will provide the required spatial resolutions of 10 μm and 50 μm in the planes perpendicular and parallel to the beam line respectively. Such detectors have been successfully implemented at the Large Electron-Positron (LEP) collider and will be used at the Large Hadron Collider (LHC).

A relativistic particle emits X-rays when traversing the interface between two mediums of different dielectric properties. This is called transition radiation and can be detected by the outer layer of the SIT with minor modifications. Transition radiation allows for particle identification, and is specifically used for good electron-pion separation. A medium with different dielectric properties to silicon can be

inserted in the space between the cylinders, and the spatial resolution of the SIT will make it an ideal transition radiation detector.

Forward Tracking Detector

Another part of the intermediate tracking system will be the Forward Tracking Detector (FTD), which will comprise of seven detectors at right angles to the beam line. The first and last detector planes will be located at distances of 20 and 130 cm respectively from the interaction point, as shown in figure 2.5. The spacings between the planes will increase with distance from the interaction point. The first three layers will comprise of silicon pixel detectors with a pixel size of 50 $\times$ 300 μm, identical to those designed for the ATLAS (A Toroidal LHC Apparatus) experiment at the LHC. Silicon strip technology of spatial resolution 25 μm will be used for the last four planes.

Time Projection Chamber

The Time Projection Chamber (TPC) is part of the central tracking system and will play a pivotal role in finding and measuring the energy loss of charged particles. To do this, it will require good solid angle coverage and track resolution. As a result it will need to be a large structure to maximise the number of points on tracks made by passing particles. However, the size of the TPC will be constrained by the tungsten mask system and the coil.

The TPC will be contained at a radius between 0.32 m and 1.7 m from the interaction point, and will be of length 2.73 m. The chamber will be filled with gas, which is likely to be a mixture of 93% argon, 2% carbon dioxide and 5% methane. This mixture will give an acceptable average transverse spatial resolution of 150 μm.

Electrons generated by passing charged particles will proceed towards a system of pads, where their signal will be amplified by high electric fields generated near thin wires. However, close to the wires the electric and magnetic fields are no longer parallel, resulting in a transverse movement of electron pairs. This leads to a deterioration of detector resolution. The magnitude of this movement is determined

by the magnetic field strength supplied by the coil. This technique has been used in past particle physics experiments where the strength of the magnetic field has been relatively small. For example, the OPAL (Omni-Purpose Apparatus at LEP) experiment immersed the tracking system in a magnetic field of 0.435 T. However, the strength of the magnetic field at TESLA will be larger and therefore a new method is needed.

Currently, there are two possible alternatives to the conventional wire chamber design: Gas Electron Multipliers (GEM); and Micromegas. These two possibilities also provide a natural supression of distortions caused by the migration of positive ions, which are released as electron pairs travel through the detector material.

Gas Electron Multipliers are currently in use at the Common Muon Proton Apparatus for Structure and Spectroscopy (COMPASS) experiment at CERN and the HERA-B experiment at the Hadron-Electron Ring Accelerator (HERA), DESY. At TESLA, the GEM will be a thin polymer foil with a coat of silicon on both sides. It will contain a high density of tiny holes at spacings of approximately 100 μm. The potential difference between the two sides will generate a strong electric field (18 kV/cm) within the holes. As the electron pairs are funnelled into these holes, their signal will be amplified and transferred to the readout pads. This will result in a restricted transverse movement of electrons and thus an improvement in spatial resolution.

The micromegas option consists of a thin metallic mesh at a distance of 50-100 μm from the plane of the readout pad. A strong electric field of 30 kV/cm can be generated in the gap, in which electrons can be amplified on their way to the readout electrodes. Although untested, the micromegas design has some distinct advantages over GEMs. It is robust, simple to construct and cheap in comparison. It also has the same advantages as GEMs have when compared with the traditional wire chamber design.

A wire chamber design has also been outlined in the unlikely event that the above two proposals fail to meet expectations.

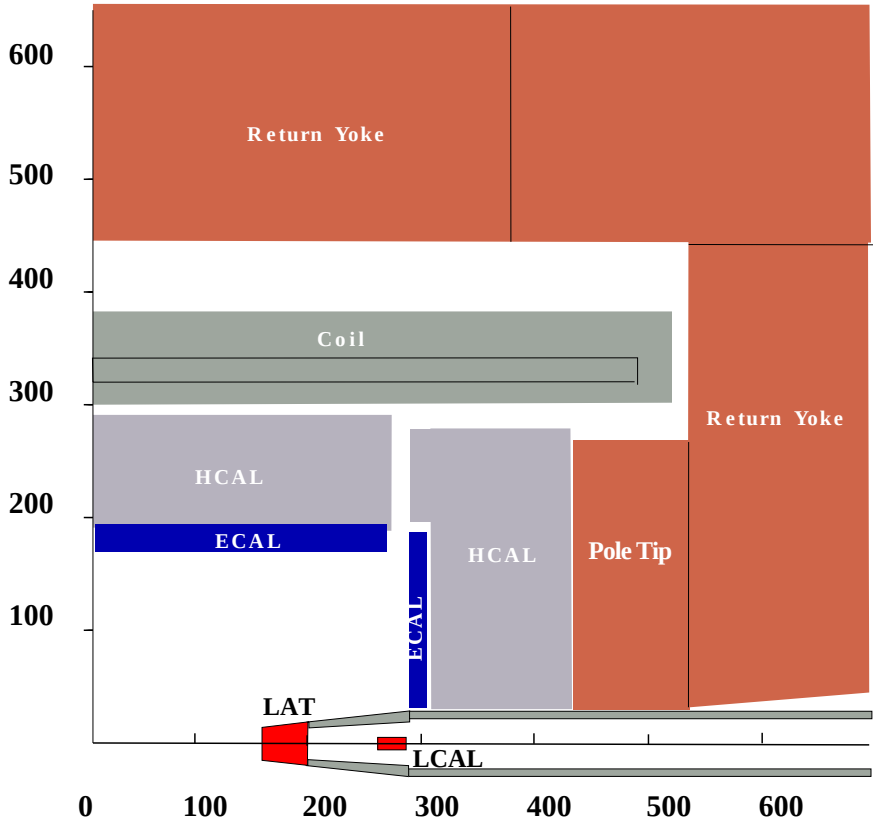

Figure 2.7: Proposed Layout of Calorimeter System at TESLA. Distances are in cm. Taken from TESLA Technical Design Report [15].

Forward Chambers

The central tracking system will also include a Forward Chamber (FCH), which will consist of 12 gas-filled straw tubes of 5 mm diameter. The chamber itself will be a 6 cm thick detector stretched over a similar radius from the beam pipe as the TPC. The 12 straws will be arranged into pairs, covering six different planes. The FCH will aid in track resolution, and each plane will provide a spatial resolution of 100-120 μm. This results in a total spatial resolution of 50 μm.

2.3.2 Electromagnetic Calorimeter

Calorimeters are instruments that detect and measure the energy and positions of particles. The proposed layout of the calorimeter system is shown in figure 2.7. The Electromagnetic Calorimeter (ECAL) will be contained within the magnetic field

generated by the Coil.

The ECAL will be responsible for the detection and measurements of electrons, positrons and photons. It will be located at a radius of 1.6 m and a distance of 2.8 m from the interaction region. There are two possible designs for the ECAL at TESLA: traditional silicon tungsten (SiW) calorimetery; and a calorimeter utilising Shashlik technology.

The traditional SiW ECAL will be comprised of a cylindrical barrel structure and two endcaps, containing finely segmented sheets of tungsten. As electrons and positrons pass through the calorimeter, they will interact with the material and pair-produce photons. These photons will in turn pair-produce electron-positron pairs, until all the energy of the initial particles has been deposited in the ECAL. Photons produce a similar effect. In the longitudinal direction, 30 layers of 0.4 X_0 thick tungsten absorbers will be placed within a space of 12 radiation lengths. The same amount of space, in the transverse direction, will contain 10 layers of 1.2 X_0 thick tungsten sheets divided into readout cells of approximate area 1 cm^2. The cross-section of the barrel will resemble a uniform octagon, each side of which is called a stave. Each stave will be divided into five modules of tungsten sheets. Layers of silicon are to be divided into 64 pads of area $1.15 \times 1.07\,\mathrm{cm}^2$ and attached to both sides of these plates. Together with the connectors, these structures are known as detection slabs. A detection slab will cover a $90 \times 160\,\mathrm{cm}^2$ area. On top of the silicon wafers, a printed circuit board will extract signals. Around 140 signals will be transferred, within a space of 1 cm, from the board to the electronics by wires of thickness 50 μm. The end cap calorimeter will be constructed from 4 similar modules. To ensure maximum coverage, two staves will overlap and the end cap calorimeter will stretch to the outer radius of the barrel region. Although the silicon diodes dissipate relatively little power, cooling is required for the readout electronics. This will be provided by cooling pipes in the space between the ECAL and the hadronic calorimeter.

Calorimeters built using Shashlik technology have a number of advantages over traditional designs, in that they are easier to assemble and operate, provide good

coverage and are relatively cheap. This technology is bound to play an important role at future positron-electron colliders. Shashlik technology makes use of the property of certain chemical compounds which emit pulses of light as charged particles or high energy photons pass through them. This phenomenon is called scintillation and these chemical compounds are scintillators. A module contains eighteen 3×6 cells. Each cell has 140 layers of 1 mm thick lead and 1 mm thick scintillator plates. This structure has a total depth of 25 X_0, of which the scintillator plates in the first 5 X_0 will consist of a scintillator with a long decay time. The scintillating material has yet to be decided, but the BC-444 scintillator has been used successfully in tests, and has a decay time of 250 ns. A standard plastic scintillator with a shorter decay time of 10 ns will be used for the remaining plates. Nine fibre optic cables will be used to carry the light signals to the back of the calorimeter. A network of cables will be set up to carry light signals outside the magnetic field so that they can be read by photomultiplier tubes. The barrel part of the calorimeter will consist of 21 modules pointing towards the interaction point and a central ring of 56 modules which will not be facing the interaction point. Two rows of 56 modules will be used to assemble the barrel, resulting in a total of 2048 modules. An endcap detector will be built using a similar arrangement.

2.3.3 Hadronic Calorimeter

The Hadronic Calorimeter (HCAL) will be responsible for the detection and measurements of hadrons. As hadrons pass through the HCAL, they will interact with the material of the detector to produce showers. These showers will produce more showers until all of the initial hadron's energy has been deposited. The HCAL will be situated at a radius of 1.9 m and a distance of 2.8 m from the interaction point, with a slight overlap with the ECAL. This will ensure that there is good solid angle coverage by both calorimeters. There are two proposals for the HCAL at TESLA. One is a tile calorimeter with analogue readout, and the other is a segmented calorimeter with a digital output.

The tile hadronic calorimeter design will consist of a barrel region divided into

16 modules and two endcaps, each containing 4 modules. The calorimeter will contain a scintillating material, operating on the same principle as the Shashlik design for the ECAL explained in section 2.3.2. A module will consist of 20 mm thick absorber plates made from a material with low magnetic permeability, such as brass or stainless steel. Gaps of depth 6.5 mm will be made in the plates into which scintillator plates can be inserted. One module will hold 38 and 53 layers in the barrel and endcap regions respectively. Each layer will be of thickness 1.15 X_0 and divided into tiles. The inner layer will contain square tiles of area 25 cm^2, which will increase to 625 cm^2 at the outer radius. Eight layers will fill the gap between the barrel and endcap modules. The total thickness of scintillator in one module will be 5 mm, with the remaining room taken up by the readout electronics and equipment. The light emitted by the scintillating layers will be transferred to a waveshifting fibre by refraction and reflection. Here the light will be absorbed, and converted from blue light to green light. The light will then be transferred to the photodetectors by fibre optic cables. Readings from these detectors will then undergo analogue-to-digital conversion.

The digital hadronic calorimeter will require cells with a very small area, so that simply counting them will provide an energy estimate. An appropriate cell size would be 1 cm^2, and the design will be based on the same structure as the tile hadronic calorimeter. The absorber plates will be made from stainless steel and the detecting medium will either consist of wire or resistive plate chambers. A design based on thin wire chambers has been proposed, which will need additional signal amplification. The main advantage of this design is that it provides better resolution than the analogue tile calorimeter, and would be an ideal partner to the SiW electromagnetic calorimeter.

2.3.4 Muon Detector

The main task of the muon detector will be to identify and measure the momentum of muons. Muons are fundamental particles which penetrate all layers of the detector, but unlike neutrinos, they do interact strongly with matter. As a result, they deposit

some energy in all areas of the detector and pass through to the final layer, as shown in figure 2.7. In addition to muon detection, the muon identifier will catch any hadronic showers which do not deposit all their energy in the HCAL. The remaining energy can be measured and added to the readings given by the hadronic calorimeter.

The iron yoke will be used as an absorber, and will be divided into slabs. It will consist of a barrel region and two endcaps. The overall thickness of the yoke required will be 1.6 m to enable the coil to provide a magnetic field of 4 T. This will help to reduce any background from hadrons that have not dissipated all of their energy in the HCAL.

The main muon detector will be situated at a radius of 6.45 m from the interaction point, and will envelop the entire detector. The complete detector will need to cover a large volume, and therefore it needs to be relatively inexpensive and reliable. As the detector will only be responsible for finding muons, large pulses can be used, which will simplify the readout electronics. A major background for this detector will be muons originating from incident cosmic rays, which can be reduced with good time resolution. There are two types of detector technologies that satisfy these requirements: Plastic Streamer Tubes (PST); and Resistive Plate Chambers (RPC).

Of these two technologies, the RPCs are the most attractive. There is no need of stretching wires and a malfunctioning wire does not affect the rest of the detector. RPCs can also be easily shaped to cover the detector, and together this makes RPC technology the first choice for the muon detector at TESLA.

Twelve planes of active detector will be located within the main barrel, with an additional 11 planes at the endcaps. The detectors would cover an area of 7000 m^2. The first 10 planes will be kept at spacings of 10 cm, with the last plane located outside the iron. They will be interspersed in 4 cm wide gaps. The main barrel would have the shape of a regular octagon and will be of total length 14.4 m. It will be divided into 3 sections of length 3.7 m, 7 m and 3.7 m respectively. The endcaps will extend at a radius of 46 cm from the beam line to the inner radius of the main barrel. The encaps will be 2 m thick. The RPC planes within the detector

will have a maximum area of approximately 4.2 m^2. The first 11 planes in the barrel region and the first 10 sheets in the endcap region will track the muons and measure their energies. An overall resolution of 1 cm can be obtained. Additionally, the iron contained within the pole tip shown in figure 2.7 can be segmented, adding an extra 5 planes of RPCs.

2.3.5 Low Angle Tagger

The Low Angle Tagger (LAT) will serve two primary functions. It will measure the energy of electrons as they approach the interaction point, and will extend the coverage of the ECAL to polar angles below 30 mrad. Placed at the ends of the Tungsten Mask, it will also help to reduce the background from bremsstrahlung and beamstrahlung effects. The LAT will consist of 63 planes of 2.6 mm tungsten and 0.5 mm silicon.

2.3.6 Luminosity Calorimeter

The Luminosity Calorimeter (LCAL) will measure the amount of background particles originating from the electron and positron beams. This information is needed for luminosity measurements. In addition, the LCAL will act as another low angle calorimeter and provide some shielding for the main detector. It will be situated within the beam pipe at a distance of 220 cm from the interaction point. Due to its location, the detector will need to be radiation hard to resist the constant flux of electromagnetic particles. The LCAL will be able to measure electron showers between the polar angles 6 mrad and 28 mrad. Sixty-three planes of tungsten absorber interspaced with 63 planes of silicon or diamond sensors of thickness 500 μm will be contained within the LCAL. Diamond has a higher threshold for the radiative effects that the LCAL will experience compared to silicon.

2.3.7 Detector at the Photon Collider

As mentioned previously, an additional optical system needs to be placed inside the detector at the second interaction point to enable beam conversion. The laser beam itself will be contained within the vertex detector and will require a clear angle of ± 78 mrad. An angle of ± 300 mrad can be provided in the vertex detector without loss of tracking resolution. Additional mirrors, including the final focusing mirror, of diameter 15-20 cm will be contained within the vertex detector at angles ranging from 120 to 140 mrad. These mirrors will be located close to the calorimeters, and therefore will not have a major impact on the detectors.

Chapter 3

The Standard Model and Supersymmetry

3.1 The Standard Model

Since its introduction in 1970, the Standard Model [17] of particle physics has been resoundingly successful in predicting the observations made in modern day experiments. In essence it is a gauge theory based on the group $\mathrm{SU}(3) \otimes \mathrm{SU}(2) \otimes \mathrm{U}(1)$. It contains 12 spin-$\frac{1}{2}\hbar$ fundamental particles, which are subdivided into equal numbers of quarks and leptons. When bound together, quarks form mesons and baryons. In addition, every particle in the Standard Model has a corresponding anti-particle. Anti-particles are identical to their counterparts in all respects, apart from the reversal of all internal quantum numbers such as charge. Particles interact by the exchange of integer-spin gauge bosons.

3.1.1 Fundamental Particles

The fundamental particles of the Standard Model are the building blocks of all matter, which means that they are not bound states of other particles. As a result, they are assumed to be point-like. A group of six quarks and six leptons form three generations of fundamental particles, of which only the first generation is stable.

Together, these fundamental particles are called fermions (spin-$\frac{1}{2}\hbar$).

Quarks

Name	Symbol	Electric Charge (e)	Mass (GeV)	Generation
down	d	$-\frac{1}{3}$	≈ 0.35	1st
up	u	$+\frac{2}{3}$	≈ 0.35	1st
strange	s	$-\frac{1}{3}$	≈ 0.5	2nd
charm	c	$+\frac{2}{3}$	≈ 1.5	2nd
beauty	b	$-\frac{1}{3}$	≈ 5.0	3rd
top	t	$+\frac{2}{3}$	174.3 ± 5.1	3rd

Table 3.1: Properties of Quarks in the Standard Model. All values are taken from [17], except the mass of the top quark, which is taken from current experimental data [18].

An outline of the properties of quarks is given in table 3.1. These spin-$\frac{1}{2}\hbar$ particles can form bound states of mesons and baryons, collectively known as hadrons. Mesons, such as the π^0 and η particles, consist of a quark and an antiquark. The proton and neutron are baryons that contain 3 quarks, each of which possess a baryon quantum number of $\frac{1}{3}$. All the quarks have anti-particles, written as $\bar{\text{u}}$ in the case of the anti-up quark, which possess the opposite electric charge and baryon number. In addition, the quarks carry a colour charge. There are three types of colour: Red; Green; and Blue, which can be held by any type of quark. Antiquarks have colour charges of Anti-Red, Anti-Green and Anti-Blue.

Leptons

The second group of fundamental particles are the leptons, whose properties are oulined in table 3.2. Each lepton carries a conserved quantum number, similar to the baryon number possessed by quarks. However, unlike quarks, each lepton generation has its own lepton conservation number. For example, the electron and

Name	Symbol	Electric Charge (e)	Mass (MeV)	Generation
electron	e^-	-1	0.5110	1st
electron neutrino	ν_e	0	0	1st
muon	μ^-	-1	105.7	2nd
muon neutrino	ν_μ	0	0	2nd
tau	τ^-	-1	1777	3rd
tau neutrino	ν_τ	0	0	3rd

Table 3.2: Properties of Leptons in the Standard Model. All values are taken from [18].

its neutrino carry an electron lepton number of 1. Anti-leptons have opposite charges and lepton numbers associated with them. Standard Model neutrinos are massless particles, and interact weakly with matter, thus making them difficult to detect.

3.1.2 Particle Interactions

There exist four possible ways for the fundamental particles to interact with each other. This occurs by way of gauge boson exchange, and each interaction has different gauge bosons associated with it.

The strong interaction affects those particles which possess a colour charge. This includes quarks and antiquarks, and is responsible for the meson and baryon bound states. The mediating gauge boson for this force is the gluon, which carries both a colour and an anti-colour charge. As gluons also possess colour charges, the strong interaction also affects them, meaning that they can couple to themselves.

Both quarks and leptons are affected by the weak interaction, which is observed in nuclear beta decay. It is mediated by the exchange of $W^\pm$ and Z bosons.

The photon is the exchange boson for electromagnetic interactions, which occur between particles with electric charge. Therefore all the quarks, the electron, the muon and the tau are affected by this force. It is responsible for holding atoms and

Name	Symbol	Electric Charge (e)	Mass (GeV)	Spin $\hbar$	Interaction
gluon	g	0	0	1	Strong
W boson	W^+	+1	80.4	1	Weak
	W^-	−1			
Z boson	Z^0	0	91.2	1	Weak
photon	γ	0	0	1	Electromagnetic
graviton	G	0	0	2	Gravitational

Table 3.3: Summary of Gauge Boson Properties and the Interactions that they mediate. All values are taken from [18].

molecules together, and at these scales, the electromagnetic force is dominant over the other interactions.

Finally, the gravitational force is responsible for the shape of the Universe. By far, it is the weakest force on the scale of individual particles, and is mediated by the as yet unobserved graviton. Attempts to incorporate this force within the Standard Model have been unsuccessful, and as such, it is not included within the framework.

The four forces of nature are summarised in table 3.3. Apart from the graviton, all the gauge bosons are spin-1 particles. Gauge theories predict massless exchange particles, in contradiction to the experimental evidence for W and Z bosons. This implies that there is an additional mechanism that generates particle masses, known as the Higgs mechanism. The Higgs Boson H^0 is the spin-0 particle associated with this mechanism, and is yet to be observed.

All interactions in the Standard Model must conserve certain quantities. These rules are known as conservation laws, and specify that energy, momentum, angular momentum, electric and colour charges, and baryon and lepton flavour numbers must be conserved in every interaction.

3.1.3 Electroweak Unification

The electroweak theory unifies the weak and electromagnetic interactions, and is based on the gauge group $\mathrm{SU}(2) \otimes \mathrm{U}(1)$.

The violation of the parity quantum number in weak interactions means that left-handed and right-handed fermions need to be treated differently. Parity non-conservation implies that unequal quantities of left- and right-handed particles are produced in an interaction. The spin of right-handed particles points in their direction of motion, and the opposite is true for left-handed particles. Therefore, left-handed fermions form SU(2) doublets and the right-handed quarks and leptons form U(1) singlets. For example, the quark eigenstates are given by:

$$\begin{aligned} \psi_1(x) &= \begin{pmatrix} u \\ d' \end{pmatrix}_L , \quad \begin{pmatrix} c \\ s' \end{pmatrix}_L , \quad \begin{pmatrix} t \\ b' \end{pmatrix}_L \\ \psi_2(x) &= u_R , \quad c_R , \quad t_R \\ \psi_3(x) &= d'_R , \quad s'_R , \quad b'_R \end{aligned}$$

where L and R represent left- and right-handed states respectively. The electroweak eigenstates differ from the mass eigenstates for quarks. The d', s' and b' states are weak interaction quark eigenstates that can be represented by their strong interaction counterparts (d, s and b) using the Cabibbo-Kobayashi-Maskawa (CKM) matrix:

$$\begin{pmatrix} d' \\ s' \\ b' \end{pmatrix} = \begin{pmatrix} V_{ud} & V_{us} & V_{ub} \\ V_{cd} & V_{cs} & V_{cb} \\ V_{td} & V_{ts} & V_{tb} \end{pmatrix} \begin{pmatrix} d \\ s \\ b \end{pmatrix} \tag{3.1}$$

where the V_{ij} components of the CKM matrix represent the relative strengths of transitions of quarks with flavour i to those with flavour j. The off-diagonal elements of the CKM matrix in equation 3.1 are non-zero terms, implying that quarks can mix between generations. As a result, the otherwise stable beauty and strange quarks are now able to decay.

Gauge theories, such as the Standard Model, use a Lagrangian density $\mathcal{L}$ to associate fields ψ with physical systems. This density satisfies the Euler-Lagrange

equation of motion:

$$\partial_\mu \left(\frac{\partial \mathcal{L}}{\partial(\partial_\mu \psi)} \right) = \frac{\partial \mathcal{L}}{\partial \psi} \ , \qquad \partial_\mu = \frac{\partial}{\partial x^\mu} \tag{3.2}$$

A relativistic wave equation for the field can be obtained by solving equation 3.2. For example, the Dirac equation is found when using the Lagrangian describing spin-$\frac{1}{2}$ particles of mass m, $\mathcal{L} = \bar{\psi}(i\partial_\mu \gamma^\mu - m)\psi$.

Interactions in the Standard Model can be described by requiring that the Lagrangian be invariant under gauge transformations. This can be illustrated with the U(1) gauge transformation for the singlets:

$$\psi(x)_R \rightarrow \psi'_R(x) = e^{i\beta(x)Y}\psi_R(x) \tag{3.3}$$

where Y is the fermion hypercharge and β is an arbitrary scalar function that defines the process. The fermion hypercharge Y is obtained from the expression $Q = I_3 + \frac{Y}{2}$, where Q is the electric charge and I_3 is the third component of the weak isospin. The arbitrary scalar function β is a function of position x, and therefore corresponds to a local transformation.

This leads to a residual term $\delta\mathcal{L}$, which implies that the Lagrangian is not invariant under this transformation:

$$\mathcal{L}' \rightarrow \mathcal{L} + \delta\mathcal{L} = \mathcal{L} - (\partial_\mu \beta(x) Y)\bar{\psi}\gamma_\mu \psi \tag{3.4}$$

To restore the invariance of the Lagrangian, a gauge field A_μ needs to be introduced, such that under a local U(1) symmetry the field will transform as:

$$A_\mu \rightarrow A'_\mu = A_\mu - \frac{1}{e}\partial_\mu \beta(x) Y \tag{3.5}$$

This extra gauge field corresponds to the photon, and results in the gauge invariant Lagrangian $\mathcal{L}_\psi$:

$$\mathcal{L}_\psi = \mathcal{L}_D - eA_\mu \bar{\psi}\gamma^\mu \psi \tag{3.6}$$

where $\mathcal{L}_D$ is the Lagrangian for the Dirac equation.

The $\mathrm{SU}(2) \otimes \mathrm{U}(1)$ gauge transformation for left-handed fermion doublets can be expressed as:

$$\psi_L(x) \rightarrow \psi'_L(x) = e^{i\alpha(x)\cdot\sigma} e^{i\beta(x)Y} \psi_L(x) \tag{3.7}$$

where α is a vector function and σ represents the Pauli spin matrices. The Lagrangian under this gauge transformation is not gauge invariant, and requires the introduction of 4 new gauge fields. The fields W^1_μ and W^2_μ couple to the weak isospin, and represent the $W^\pm$ bosons. The photon and Z^0 boson are mixtures of the W^3_μ and B_μ gauge fields:

$$\begin{pmatrix} A_\mu \\ Z_\mu \end{pmatrix} = \begin{pmatrix} \cos\theta_W & \sin\theta_W \\ -\sin\theta_W & \cos\theta_W \end{pmatrix} \begin{pmatrix} B_\mu \\ W^3_\mu \end{pmatrix} \tag{3.8}$$

where θ_W is the weak mixing angle, which determines the relative strengths of the weak and electromagnetic interactions.

3.1.4 Quantum Chromodynamics

The strong interactions between quarks and gluons are described by a $\mathrm{SU}(3)$ gauge theory called Quantum Chromodynamics (QCD). An example of the strong force is an interaction between a green quark and a blue quark within a baryon. The green quark will be attracted to the blue quark and will emit a gluon carrying anti-blue and green colour charges, which are absorbed by the blue quark. This results in the blue quark gaining green colour charge and losing its blue colour. Quarks of the same colour repel each other by emiting a gluon of anti-colour and colour charge. Unlike the weak and electromagnetic interactions, the strong force becomes stronger with distance.

There are a total of 8 gluons, which are represented by the field A^a_μ. The Lagrangian for the strong interaction is:

$$\mathcal{L} = q^{-i} \left[i\partial\delta^j_i - m\delta^j_i - \alpha_s(Q^2) A^a_\mu \gamma^\mu (T^a)^j_i \right] q_j \tag{3.9}$$

where the indices i and j represent the colour of the quarks involved in the interaction, and γ^μ denotes a set of four Dirac γ-matrices. The strong coupling constant is $\alpha_s(Q^2)$, which is dependent on the momentum transfer Q^2 between the quarks. As the distance between the quarks increases, Q^2 decreases, resulting in a large α_s. This is the reason for quark confinement within a nucleon. Eventually, the potential energy between the two quarks is large enough to create a new quark-antiquark pair. The generator of the SU(3) group is the $T^a = \frac{1}{2}\lambda^a$ term, where λ^a are the eight 3×3 Gell-Mann matrices.

This means that individual quarks cannot exist independently, as only colourless objects can survive in isolation. When quarks are produced in isolation from particle decay, they generate more quarks and anti-quarks, resulting in bound states of mesons and baryons. This process is called hadronisation.

A more rigorous theoretical treatment of the Standard Model is given in [19].

3.2 Problems with the Standard Model

Although the Standard Model has been successful in explaining the observations made in particle physics experiments, it is not a complete theory as it leaves many questions unanswered. For example, the Standard Model does not explain the reasons behind fermion masses and the existence of 3 generations of quarks and leptons. There are also strong theoretical reasons that indicate that there may be a more fundamental theory, of which the Standard Model is just a low energy approximation.

Recent experimental results [20] from the Super-Kamiokande experiment indicate that neutrinos do mix, and therefore they must have a mass. Neutrino mixing was first postulated to explain the apparent difference between experimental measurements and theoretical predictions for the flux of incident neutrinos on Earth from the Sun. If neutrinos were massless, they would not be able to mix between generations.

There exists a large matter-antimatter asymmetry in the Universe, which seems

to be in contradiction to the standard cosmological model. The theory of the birth of the Universe is referred to as the Big Bang Model. It states that at the time of initial expansion, the Universe was comprised of equal matter and anti-matter particles. Therefore, some process must have occured to change the present day Universe into a matter-dominated one. In 1967, the Sakharov conditions [21] were proposed to explain the criteria required for the current nature of the Universe. One of these conditions was the violation of baryon number, which is a conserved quantity in the Standard Model. If the Standard Model is correct, then there must always have been an excess of matter, in disagreement with the Big Bang Model.

As mentioned in section 3.1.2, the gravitational force is very weak on the atomic scale and is not included in the Standard Model. However, quantum gravitational effects become important at the temperatures and densities present in the early Universe. The properties of the early Universe are defined by the Planck scale, where quantum gravitational effects become important at energies of 1.2×10^{19} GeV. It is unreasonable to assume that there is no new physics between current collider energies and the Planck energy.

The mass hierarchy problem [22, 23] arises from the radiative corrections to particle masses δm, resulting from energy losses and particle production. For example, a fermion can emit and re-absorb a photon, resulting in the logarithmically divergent mass corrections [23]:

$$\delta m_f \approx \frac{3\alpha}{4\pi} m_f \ln\left(\frac{\Lambda^2}{m_f^2}\right) \tag{3.10}$$

where m_f is the mass of the fermion and α is the electromagnetic coupling constant. The scale up to which the Standard Model remains valid is represented by Λ. When the Planck mass is substituted into equation 3.10, the radiative corrections remain relatively small, $\delta m \leq m_f$.

However, particles that are described by a scalar field, such as the Higgs boson, require quadratically divergent mass corrections [22]:

$$\delta m_H^2 \approx C_H \frac{\lambda}{16\pi^2} \Lambda^2 \tag{3.11}$$

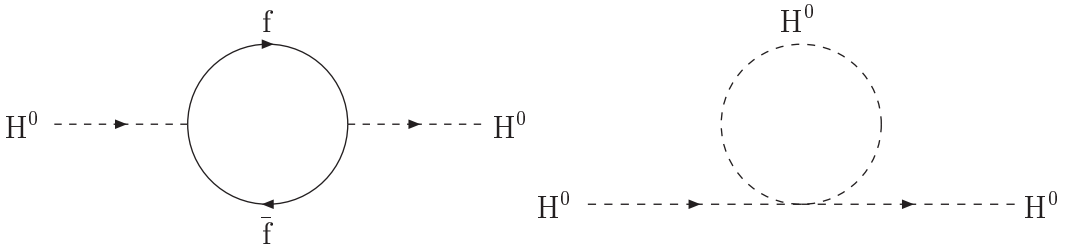

Figure 3.1: Feynman Diagrams illustrating the One-Loop Radiative Corrections to the Higgs Mass. The examples shown above are fermion (f) pair-production and annihilation, and Higgs boson (H^0) emission and reabsorption.

where C_H is a dimensionless constant and λ is a coupling constant. These corrections correspond to the loop diagrams in figure 3.1. From the measured masses of the gauge bosons, the mass of the Higgs boson must be of the same order as that of the $W^{\pm}$ boson. However, the introduction of the Planck scale leads to vast radiative corrections due to the difference between the $W^{\pm}$ boson and Planck masses.

These radiative corrections are very large compared with the expected mass of the Higgs bosons, implying that the mass of the Higgs boson is divergent. Although these terms can be added into the Standard Model Lagrangian to cancel the divergencies, this requires fine tuning, and is considered unnatural. In order to avoid this fine tuning, Λ should be less than 1 TeV [23], indicating that there is some new physics at this scale.

3.3 An Extension to the Standard Model

The theory of supersymmetry attempts to solve these problems. As an extension to the Standard Model, a requirement of supersymmetry [24] is that the equations of the Standard Model remain unaltered when bosons are replaced by fermions, and vice versa. The theory can be viewed as a quantum operator $\hat{Q}$, such that:

$$\begin{aligned} \hat{Q}|\text{Boson}\rangle &= |\text{Fermion}\rangle \\ \hat{Q}|\text{Fermion}\rangle &= |\text{Boson}\rangle \end{aligned} \tag{3.12}$$

The operator in equation 3.12 changes the spin of a particle by at least half a

unit, implying that $\hat{Q}$ is a fermionic operator. This can be represented by several 2-component Weyl-spinors Q^i_α, where $i = 1, \ldots, N$. Being a symmetry operator, Q^i_α and its anti-commutator $\{Q^i_\alpha, Q^j_\beta\}$ must commute with the Hamiltonian H:

$$[Q^i_\alpha, H] = 0 \quad \text{and} \quad [\{Q^i_\alpha, Q^j_\beta\}, H] = 0 \tag{3.13}$$

The simplest example of a supersymmetric theory is one with a single operator Q_α, or in other words when $N = 1$. For a massless particle, a momentum-energy tensor can be chosen such that $P_\mu = \frac{1}{4}(-1, 0, 0, 1)$. This is a four-dimensional vector which gives the particle a momentum component of $-\frac{1}{4}$ in the x-direction and an energy component of $\frac{1}{4}$. For the simplest case, the following commutation relations can be derived [23, 25]:

$$\{Q_\alpha, Q^\dagger_{\dot{\beta}}\} = 2\sigma^\mu_{\alpha\dot{\beta}} P_\mu \tag{3.14}$$

$$\{Q_\alpha, Q_\beta\} = \{Q^\dagger_{\dot{\alpha}}, Q^\dagger_{\dot{\beta}}\} = 0 \tag{3.15}$$

$$[Q_\alpha, P_\mu] = [Q^\dagger_{\dot{\alpha}}, P_\mu] = 0 \tag{3.16}$$

where σ^μ represents the Pauli matrices. In the case of the massless particle outlined previously, it is clear that the only non-vanishing relation is $\{Q_1, Q^\dagger_1\} = 1$, from equation 3.14. As a result, for a massless particle in spin state $|\lambda\rangle$, there exist two operators that will result in a non-vanishing state. These are Q_1, which will raise the spin state by $\frac{1}{2}$, and $Q^\dagger_1$, which will have the opposite effect.

3.3.1 Sparticles

In the relativistic limit, all particles can be classed as massless. Therefore, using the ideas given previously, two sets of supermultiplets can be formed. The chiral supermultiplet relates spin-$\frac{1}{2}$ fermions with scalar bosons:

$$\begin{pmatrix} \frac{1}{2} \\ 0 \end{pmatrix} \implies \begin{pmatrix} l\,(lepton) \\ \tilde{l}\,(slepton) \end{pmatrix} \quad \text{or} \quad \begin{pmatrix} q\,(quark) \\ \tilde{q}\,(squark) \end{pmatrix} \tag{3.17}$$

Name	Symbol	Mass (GeV)	Spin	Standard Model Partner
sbeauty (scalar beauty)	$\tilde{b}$	> 81.9	1	beauty quark
stop (scalar top)	$\tilde{t}$	> 95.7	1	top quark
neutralino*	$\tilde{\chi}^0$	$> 46^{\ddagger}$	$\frac{1}{2}$	none
chargino†	$\tilde{\chi}^{\pm}$	$> 94^{\ddagger}$	$\frac{1}{2}$	none

*Mixture of the photino ($\tilde{\gamma}$), Zino ($\tilde{Z}^0$) and neutral higgsinos ($\tilde{H}^0$, $\tilde{h}^0$)

†Mixture of the Wino ($\tilde{W}^{\pm}$) and charged higgsino ($\tilde{H}^{\pm}$)

‡Lower mass limit for lightest sparticle

Table 3.4: Properties of Sparticles referred to in this Dissertation. The mass limits are taken from current experimental data [18].

where the superpartners of the leptons and quarks are called sleptons and squarks respectively. Sleptons and squarks are also known as scalar leptons and scalar quarks. The vector or gauge supermultiplet relates fermions with spin-1 vector bosons:

$$\begin{pmatrix} 1 \\ \frac{1}{2} \end{pmatrix} \implies \begin{pmatrix} gauge\,boson \\ gaugino \end{pmatrix} \tag{3.18}$$

where the gaugino is the general name for the superpartners of the gauge bosons. There is also a graviton supermultiplet, which comprises of the spin-2 graviton and the spin-$\frac{3}{2}$ gravitino.

These superpartners cannot be Standard Model particles as their quantum numbers do not match. For example, integer spin gauge bosons possess a lepton number of zero, in contrast to electrons, which possess an electron lepton number of $L_e = 1$. Therefore, the sleptons, squarks and gauginos must be new particles, which are collectively known as sparticles. An outline of the properties of sparticles which are used in this dissertation is given in table 3.4.

The inclusion of new superparticles means that for every fermion loop, there is a boson loop which adds counter terms to the equations for radiative corrections. These cancel out the divergent terms without the need of fine tuning, thus solving the mass hierarchy problem oulined in section 3.2.

3.3.2 R-Parity

In addition to the quantum numbers inherited from the Standard Model, particles also possess R-parity [26, 27] in some supersymmetric theories. A particle with baryon number B, lepton number L and spin S has an R-parity of:

$$\mathcal{R}_p = (-1)^{3B+L+2S} \tag{3.19}$$

All Standard Model particles possess $\mathcal{R}_p = +1$, and all supersymmetric particles carry the opposite value. In many supersymmetric theories, R-parity needs to be conserved to account for baryon and lepton number conservation in the Standard Model. If R-parity is not violated, interactions involving supersymmetric particles must obey 3 rules:

- Supersymmetric particles are produced in pairs from Standard Model particle interactions.
- One sparticle is produced when an unstable supersymmetric particle decays.
- The Lightest Supersymmetric Particle (LSP) is stable as there is no lighter sparticle that can be produced from its decay.

Combined, this means that sparticles produced from collisions at TESLA will result in a final state containing at least two LSPs. Feynman diagrams for superparticle decays which violate [27] R-parity are shown in figure 3.2.

3.3.3 Supersymmetry Breaking

From equation 3.16, the commutation relationship $[Q_\alpha, P \cdot P] = 0$ can be derived. As the mass of a patricle is given by $M^2 = E^2 - p^2$, where E and p are the energy and momentum of the particle respectively, the relationship $[Q_\alpha, M^2] = 0$ can be inferred. Therefore, a superparticle should have the same mass as its Standard Model partner. If this is the case, there should already be experimental evidence for supersymmetry. However, supersymmetric particles are yet to be observed in particle physics experiments, which indicates that they have different masses. This

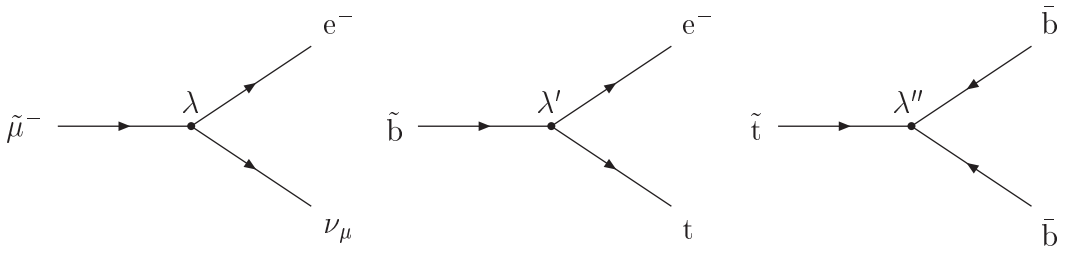

Figure 3.2: Feynman Diagrams illustrating possible R-parity Violating Decays. The Yukawa coupling constants, λ and λ' violate lepton number, and λ'' violates baryon number. These coupling constants are present in the equation for the superpotential of the supersymmetric field, and are eliminated if R-parity is conserved. If R-parity is violated, the above decays will only occur if kinematically possible.

is shown by the experimental mass limits given in table 3.4. As a result, there must be a breaking mechanism which prevents supersymmetry from being a perfect symmetry.

There are two ways in which supersymmetry breaking can be incorporated into the supersymmetric Lagrangian. It can either be explicit, meaning that it is present in the Lagrangian of the theory, or spontaneous, where it is induced by a vacuum state. Spontaneous supersymmetry breaking [28] is favoured as it is similar to the way gauge symmetry is broken and raises no conflict with supergravity theory, which attempts to incorporate the gravitational interaction. Every supersymmetric theory is based on the Lagrangian:

$$\mathcal{L} = \mathcal{L}_{SUSY} + \mathcal{L}_{SUSY\,breaking} \tag{3.20}$$

which contains a supersymmetry (SUSY) and SUSY breaking part. Although the masses of particles and their superpartners differ, it is still possible to cancel the divergences which arise in the mass hierarchy problem. This is done by inserting weak scale mass terms into the SUSY breaking Lagrangian, and is known as soft symmetry breaking.

3.4 The Minimal Supersymmetric Standard Model

Many theories of supersymmetry exist, of which the Minimal Supersymmetric Standard Model (MSSM) [23, 29] is the simplest. It is so named because of its minimal field content and superpotential, and the latter can be defined as [28]:

$$W = \sum_{L,E^C} \lambda_L L E^C H_1 + \sum_{Q,U^C} \lambda_U Q U^C H_2 + \sum_{Q,D^C} \lambda_Q Q D^C H_1 + \mu H_1 H_2 \qquad (3.21)$$

where left-handed doublets for quarks and leptons are represented by Q and L respectively. Right-handed singlets for the electron, and up and down quarks are indicated by their left-handed conjugate fields E^C, U^C and D^C respectively. The quark doublets and singlets are introduced in section 3.1.3. The 3×3 matrices in flavour space are represented by the symbols λ_L, λ_U and λ_D. These matrices are known as the Yukawa couplings, and when diagonalised, yield the CKM matrix (Equation 3.1) mixing angles and mass eigenstates.

There are two Higgs doublets, H_1 and H_2, in equation 3.21 which are a necessary addition to the MSSM [30]. In the Standard Model, there exists only one Higgs doublet, leading to one scalar field. The additional Higgs doublet in supersymmetric theory results in 5 new Higgs bosons. These comprise of 2 scalars (h^0 and H^0), one pseudo-scalar (A^0) and 2 charged scalars ($H^{\pm}$), each of which have their own superpartner. The Standard Model Higgs boson is often given the symbol h^0, which is different from that used previously. To prevent confusion, the symbol H^0 will be used to denote the Standard Model Higgs boson in this dissertation. The higgsino mass parameter μ and the ratio of Higgs expectation values $\tan\beta$ are free parameters in the MSSM, which determine the masses of the five Higgs bosons.

The MSSM consists of 124 independent parameters [29], which include the nineteen free parameters of the Standard Model. Although the parameter space is increased, experimental results can be used to rule out certain values. In addition, supersymmetry is only regarded as an extension of the Standard Model, and is likely

to form part of a more fundamental theory that will address the parameter problem. The three gaugino masses M_1, M_2 and M_3 are associated with the U(1), SU(2) and SU(3) subgroups respectively, and are the most important parameters in the MSSM.

R-parity conservation is incorporated in the constrained Minimal Supersymmetric Standard Model (cMSSM). Extensions of the MSSM [27, 28, 31], through an increase of the parameter space, can allow for R-parity violating interactions whilst accomodating the observed baryon and lepton number conservation. The constrained model forms the basis of this dissertation, and will be referred to as the MSSM.

3.4.1 Spontaneous Breaking of the MSSM

As mentioned in section 3.3.3, spontaneous supersymmetry breaking is the prefered choice. However, when attempting to construct a model based solely on the interactions between MSSM particles, problems arise from the Dimopoulos-Georgi sum rule [32]. For the first generation of fermions and their superpartners sfermions, the sum rule yields [33]:

$$\begin{aligned} m^2_{\tilde{e}_L^-} + m^2_{\tilde{e}_R^-} - 2m^2_{e^-} + m^2_{\tilde{\nu}_L} + m^2_{\tilde{\nu}_R} - 2m^2_{\nu} &= 0 \\ &= m^2_{\tilde{u}_L} + m^2_{\tilde{u}_R} - 2m^2_{u} + m^2_{\tilde{d}_L} + m^2_{\tilde{d}_R} - 2m^2_{d} \end{aligned} \tag{3.22}$$

where each first generation fermion and sfermion has three terms. These represent the square of the masses for the left-handed sfermion, right-handed sfermion and the fermion respectively. The first generation superparticles are the selectron $\tilde{e}$, sneutrino $\tilde{\nu}$, scalar up $\tilde{u}$ and scalar down $\tilde{d}$ quarks. Equation 3.22 implies that sparticles are lighter than their Standard Model counterparts, which is in contradiction to experimental observations.

A solution to this problem is presented when the existence of a hidden sector of superfields is postulated. The particles within this hidden sector do not possess gauge or superpotential couplings to any MSSM particles, all of which are contained within the visible sector. Spontaneous supersymmetry breaking occurs in the hidden sector, and is transmitted into the visible sector.

There exist two primary mechanisms [33] for transmitting supersymmetry breaking to the visible sector of the MSSM. Although the gravitational force is very weak on atomic scales, gravity mediated supersymmetry breaking [34] utilises the fact that all particles are affected by this interaction. In other words messages are sent between the hidden and visible sectors by the exchange of gravitons. In this scenario, the superpartner of the graviton, the gravitino $\tilde{\mathrm{G}}$, has a mass close to the electroweak scale. The strength of its couplings are of the order of the Planck scale, meaning that it will not be observed in particle physics experiments. This mechanism successfully incorporates the gravitational force into the MSSM, using $N = 1$ Supergravity (SUGRA) [35] theory.

Another mechanism is Gauge Mediated Supersymmetry Breaking (GMSB) [36], where the breaking of supersymmetry is transmitted to the visible sector by particles which are part of a separate messenger sector. The messenger sector consists of particles with Standard Model quantum numbers, and the gravitino has a mass in the 1-10^3 eV range. The gravitino couplings are significantly stronger than they would be in the SUGRA model.

3.4.2 Experimental Evidence

There is currently no direct experimental evidence for the existence of supersymmetry. However, the MSSM can be combined with Grand Unified Theories (GUTs), which attempt to unify the strong, electromagnetic and weak forces. Therefore, predictions can be made for the values of some parameters that can be determined experimentally.

The strong coupling constant has been found to decrease with an increase in momentum transfer Q^2 during an interaction. The electromagnetic and weak forces have been successfully unified, as outlined in section 3.1.3, and their coupling constants are found to increase with Q^2. The coupling constants merge at $\approx 10^{16}$ GeV, and meet only when supersymmetric loops are taken into account. The values for gauge interaction strengths determine the energy scale at which the coupling constants meet, and using this information, a value for the weak mixing angle can be

determined. The MSSM predicts a value of $\sin^2\theta_W \approx 0.232$ [28], which is in good agreement with the recent experimental value from LEP [37]. Other GUTs, such as the Georgi-Glashow model [38], predict a lower value for the weak mixing angle.

Baryon number is violated in GUTs through new gauge bosons, which can change quarks into leptons. This satisfies the first Sakharov condition [21], thus helping to explain the matter-antimatter asymmetry problem outlined in section 3.2. The proton, being the lightest baryon, can decay in GUTs. Experimental evidence indicates the proton lifetime is $> 10^{31}$ years [18], which does not rule out values predicted by supersymmetric GUTs of $\approx 10^{33}$ years [39].

3.4.3 Stop Squark Masses and Mixing

The determination of mass outlined below is applicable for all sfermions, but it is covered in the context of the scalar top quark as this is the subject matter of this dissertation.

Stops are scalar bosons, which means that they do not exist in left- and right-handed states. Therefore, the $\tilde{t}_L$ and $\tilde{t}_R$ particles correspond to t_L and t_R Standard Model quarks respectively. Unlike their Standard Model counterparts, the $\tilde{t}_L$ and $\tilde{t}_R$ are two distinct particles that can possess different masses. They can mix, and the stop mass matrix is given by [23, 28, 40]:

$$M^2_{\tilde{t}} = \begin{pmatrix} m_t^2 + m^2_{Q_3} + D^2_{\tilde{t}_L} & m_t(A_t - \mu\cot\beta) \\ m_t(A_t - \mu\cot\beta) & m_t^2 + m^2_{U_3} + D^2_{\tilde{t}_R} \end{pmatrix} \tag{3.23}$$

where $D^2_{\tilde{t}_L} = m^2_{Z^0}\cos 2\beta(\frac{1}{2} - \frac{2}{3}\sin^2\theta_W)$ and $D^2_{\tilde{t}_R} = m^2_{Z^0}\cos 2\beta(\frac{2}{3}\sin^2\theta_W)$. Soft supersymmetry breaking parameters for the $\tilde{t}_L$ and $\tilde{t}_R$ are represented by m_{Q_3} and m_{U_3} respectively. The H^0-$\tilde{t}_L$-$\tilde{t}_R$ trilinear coupling coefficient is A_t. For fermions other than the up, charm and top quarks, the off-diagonal terms are $m_f(A_f - \mu\tan\beta)$. The matrix yields the stop mass eigenstates [23]:

$$\begin{aligned} \tilde{t}_1 &= \tilde{t}_R\sin\theta_{\tilde{t}} + \tilde{t}_L\cos\theta_{\tilde{t}} \\ \tilde{t}_2 &= \tilde{t}_R\cos\theta_{\tilde{t}} - \tilde{t}_L\sin\theta_{\tilde{t}} \end{aligned} \tag{3.24}$$

where $\theta_{\tilde{t}}$ is the stop mixing angle. Due to the relatively large mass of the top quark compared with the other fermions, mixing between the mass eigenstates will be very large. Therefore, the lighter mass eigenstate $\tilde{t}_1$ is likely to be the lightest squark, making it an important particle to investigate.

A 180 GeV/c^2 scalar top quark has several decay modes open to it, which depend on the values of some MSSM parameters that affect the stop, chargino and neutralino masses. Assuming that the $\tilde{t}_1$ is the lightest squark, these decay channels are outlined below.

Beauty-Chargino Two-Body Decay Channel

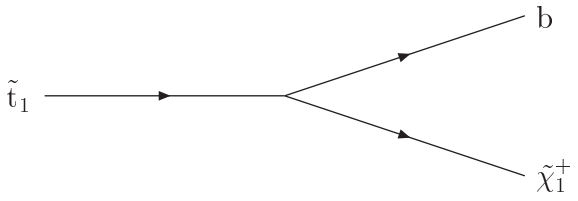

Figure 3.3: Feynman Diagram for the Decay $\tilde{t}_1 \rightarrow b\tilde{\chi}_1^+$.

The masses of the chargino $m_{\tilde{\chi}_1^+}$ and beauty quark m_b determine whether this decay chain is kinematically possible. In other words, if the mass of the scalar top quark $m_{\tilde{t}} > m_{\tilde{\chi}_1^+} + m_b$, this decay chain will dominate [41]. If $\tilde{t}_1$ is the lightest squark, the decay of the chargino will result in 3 resultant particles, one of which will be the neutralino. The other two products will either be a lepton-neutrino or an opposite flavour quark-antiquark pair.

Beauty-Neutralino-W Boson Three-Body Decay Channel

There are 3 different processes [42] for stop squark decay to a final state of $bW^+\tilde{\chi}_1^0$. If the $\tilde{t}_1$ is considered to be the lightest squark, the process shown in figure 3.4(a) is not kinematically possible, as the sbeauty scalar quark is heavier than its parent. The decay chain shown in figure 3.4(c) cannot occur for a 180 GeV/c^2 stop squark, as it would require $m_{\tilde{\chi}_1^0} \leq 5\,\text{GeV/c}^2$, which is smaller than its lower mass limit

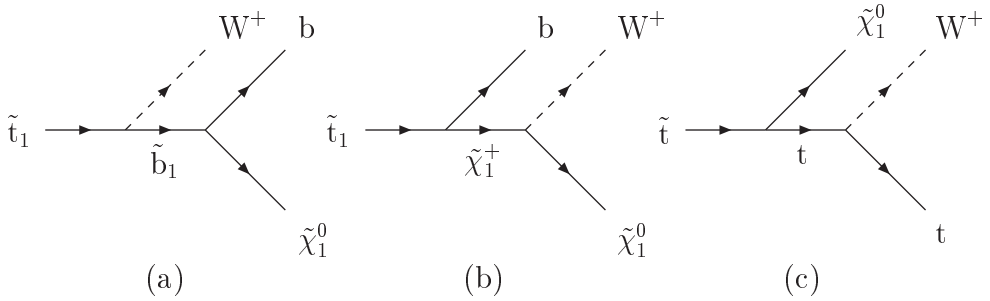

Figure 3.4: Feynman Diagrams for the Decay $\tilde{t}_1 \rightarrow bW^+\tilde{\chi}_1^0$, with the initial two-body processes: (a) $\tilde{t}_1 \rightarrow W^+\tilde{b}_1$; (b) $\tilde{t}_1 \rightarrow b\tilde{\chi}_1^+$; and (c) $\tilde{t}_1 \rightarrow t\tilde{\chi}_1^0$.

shown in table 3.4. The sequence shown in figure 3.4(b) is similar to the two-body beauty-chargino decay, and dominates when $m_b + m_{W^\pm} + m_{\tilde{\chi}_1^0} < m_{\tilde{t}_1} < m_{\tilde{\chi}_1^0} + m_t$ [41].

Charm-Neutralino Two-Body Decay Channel

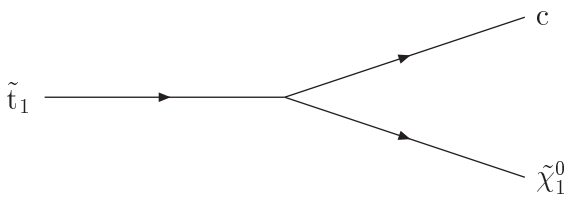

Figure 3.5: Feynman Diagram for the Decay $\tilde{t}_1 \rightarrow c\tilde{\chi}_1^0$.

The decay $\tilde{t}_1 \rightarrow c\tilde{\chi}_1^0$ [43] for a $180\,\mathrm{GeV/c^2}$ stop squark will dominate if the previous channels discussed are not kinematically possible [41]. In the MSSM, the LSP is the lightest neutralino, meaning that R-parity conservation prevents it from decaying. As the LSP is a weakly interacting particle, the signature for the decay shown in figure 3.5 is a large missing energy and two charm-jets. Scalar top pair-production and decay by this process is investigated in this dissertation.

It is worthwhile mentioning that if kinematically allowed, the strong force decay $\tilde{t}_1 \rightarrow t\tilde{g}$ is dominant over the above processes [44]. Although limits on the mass of the gluino have been achieved [18] in the high mass region, this does not rule out the possiblity of $m_{\tilde{g}} \leq 5\,\mathrm{GeV/c^2}$. In the MSSM, the neutralino is thought of as the

lightest sparticle, whose lower mass limit rules out this possibility.

3.4.4 Neutralinos

In addition to the superpartners of Standard Model particles, four new neutral spin-$\frac{1}{2}$ fermions are present in the MSSM. These particles are known as neutralinos, and form 4 mixed states comprised of two neutral higgsinos and gauginos. The photino $\tilde{\gamma}$, Zino $\tilde{Z}^0$ and higgsinos $\tilde{H}^0$ and $\tilde{h}^0$, are the superpartners of the photon, Z^0-, H^0- and h^0-bosons. The four mass eigenstates of the neutralino are denoted by $\tilde{\chi}_i^0$, where $i = 1, \ldots, 4$. The lightest mass eigenstate is represented by $\tilde{\chi}_1^0$, and can be calculated from the mass mixing matrix [23, 45]:

$$M_{\tilde{\chi}^0} = \begin{pmatrix} M_1 & 0 & -M_{Z^0} s_{\theta_W} c_\beta & M_{Z^0} s_{\theta_W} s_\beta \\ 0 & M_2 & M_{Z^0} c_{\theta_W} c_\beta & -M_{Z^0} c_{\theta_W} s_\beta \\ -M_{Z^0} s_{\theta_W} c_\beta & M_{Z^0} c_{\theta_W} c_\beta & 0 & -\mu \\ M_{Z^0} s_{\theta_W} s_\beta & -M_{Z^0} s_{\theta_W} s_\beta & -\mu & 0 \end{pmatrix} \tag{3.25}$$

where $s_\beta = \sin\beta$, $c_\beta = \cos\beta$, $s_{\theta_W} = \sin\theta_W$ and $c_{\theta_W} = \cos\theta_W$. As is clear from equation 3.25, the masses and couplings of the neutralinos depend on the U(1) (M_1) and SU(2) (M_2) gaugino masses, the ratio of Higgs vacuum expectation values ($\tan\beta = \frac{\nu_2}{\nu_1}$) and the higgsino mass parameter (μ). The vacuum expectation values ν_1 and ν_2 are obtained from the Higgs doublets [23]:

$$\langle H_1 \rangle = \begin{pmatrix} \nu_1 \\ 0 \end{pmatrix} \qquad \langle H_2 \rangle = \begin{pmatrix} 0 \\ \nu_2 \end{pmatrix} \tag{3.26}$$

In the minimal Supergravity (mSUGRA) scenario of the MSSM, outlined in section 3.4.1, the $\tilde{\chi}_1^0$ is the LSP. Astronomical observations have indicated that the vast majority of matter in the Universe is non-baryonic. This matter is weakly interacting and does not emit any electromagnetic radiation making it difficult to detect, giving it the name dark matter. If the neutralino is the LSP, and R-parity is conserved, the $\tilde{\chi}_1^0$ is a possible dark matter candidate [46].

Chapter 4

Monte Carlo Event Generation

Monte Carlo simulations portray the behaviour of physical systems by simulating these processes, rather than with the use of the differential equations that describe the system. Monte Carlo programs take random samples from probability density functions, which are descriptions of the evolution of the physical system. This procedure is repeated many times, after which the mean value is taken.

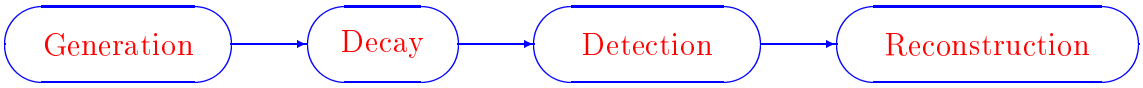

Figure 4.1: Order of Sub-Processes for One Event. Monte Carlo event generators are used to generate and decay particles, and additional programs detect and reconstruct these events.

A variety of computer programs are used in this dissertation, dividing each event into sub-processes as shown in figure 4.1. Photon-photon collisions and the decay of resultant particles are simulated using Monte Carlo event generators. Employing different Monte Carlo generators for the first two sub-processes is done in an attempt to invoke a complexity similar to that present in a physical system.

Information concerning the decay products is then conveyed to a detector program, which includes an algorithm to reconstruct the jets emitted when isolated quarks hadronise.

4.1 Particle Pair-Production

Compton-backscattered photon-photon interactions result in distributions of centre-of-mass energies, as mentioned in section 2.2.1. The invariant mass of the pair of interacting photons affects the cross-section for particle production. Two different routines were used in an attempt to describe the photon-energy spectrum for signal and background processes.

4.1.1 Vector Meson Dominance

Direct photon-photon interactions occur when two bare photons collide at the interaction point. Before colliding, a photon can fluctuate into the particles outlined below. This implies that collisions at the interaction point are not completely comprised of direct photon-photon processes.

The photon's internal structure is thought to be similar to that of hadrons, and becomes apparent at high energies on the GeV scale. There exists an interaction which allows a photon to transform into a vector meson. This is a spin-1 two-quark bound state, such as the ρ^0, ω and ϕ, so the alteration satisfies spin conservation. Before the photon beams reach the interaction point, some photons will metamorphose into vector mesons, which will interact by the strong force with other vector mesons. This enhances the quark-antiquark pair-production cross-section, and is known as Vector Meson Dominance (VMD) [47].

In addition to VMD, at high enough energies the photon can pair-produce quark-antiquark pairs before reaching the interaction point. Together with VMD, these anomalous couplings make a significant contribution to the cross-section for quark-antiquark pair production [48]. Feynman diagrams for some of the possible processes are shown in figure 4.2.

4.1.2 Stop-Antistop Pair-Production

Cross-sections for $\gamma\gamma \to \tilde{t}\bar{\tilde{t}}$ are calculated with a computer program [49] designed to generate total cross-sections for any sfermion type. The program uses the Ginzburg

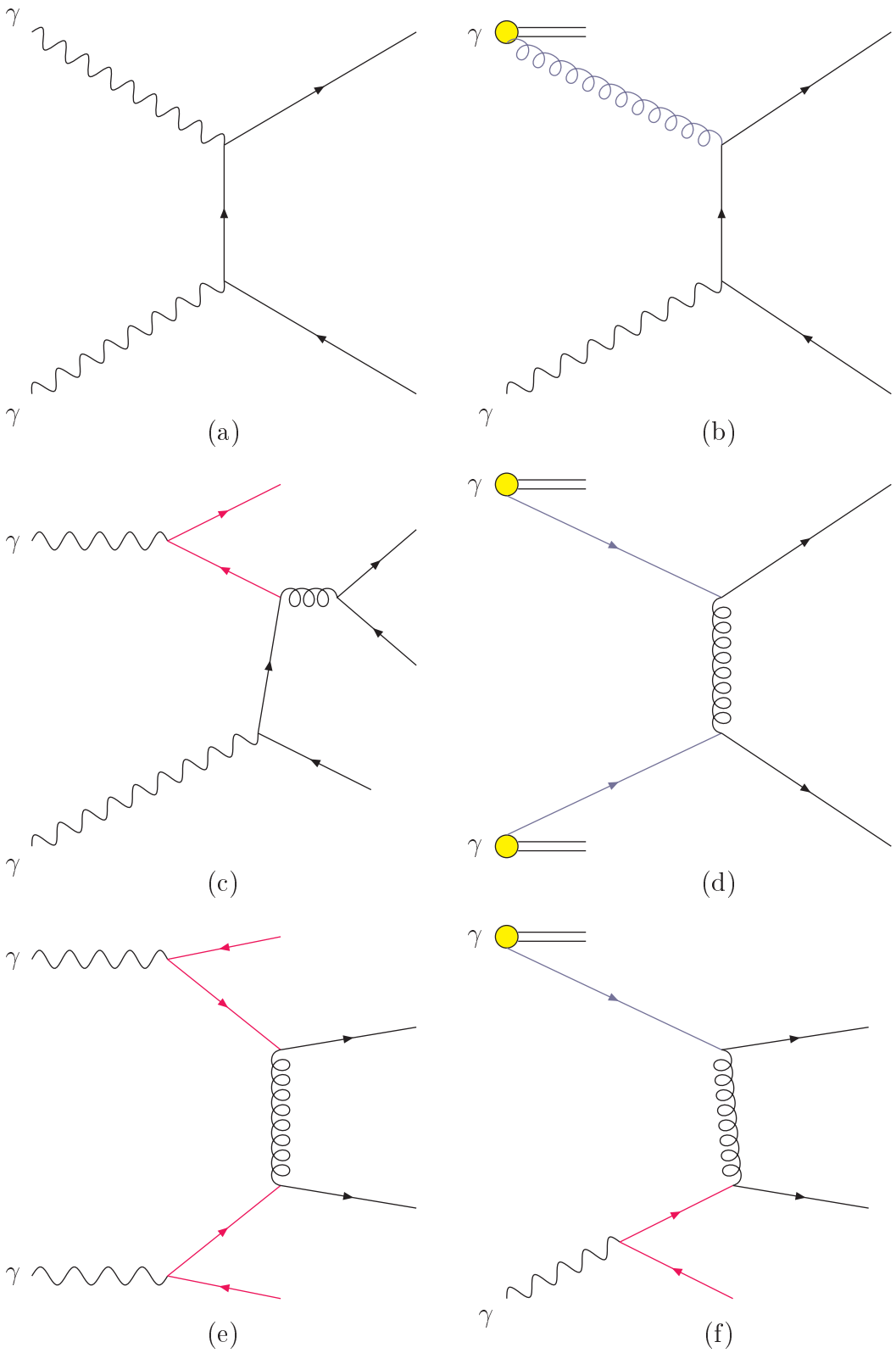

Figure 4.2: Feynman Diagrams illustrating Possible Particle Production Mechanisms in Photon-Photon Collisions: (a) direct-direct; (b) direct-VMD; (c) direct-anomalous; (d) VMD-VMD; (e) anomalous-anomalous; and (f) VMD-anomalous.

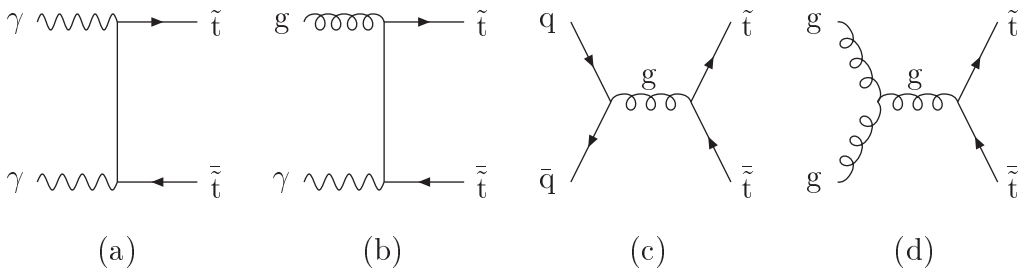

Figure 4.3: Leading Order Feynman Diagrams for Direct, Single- and Double-Resolved Scalar Top Pair-Production in Photon-Photon Interactions: (a) $\gamma\gamma \to \tilde{t}\bar{\tilde{t}}$; (b) $g\gamma \to \tilde{t}\bar{\tilde{t}}$; (c) $q\bar{q} \to g \to \tilde{t}\bar{\tilde{t}}$; (d) $gg \to g \to \tilde{t}\bar{\tilde{t}}$. A complete set of leading order Feynman diagrams is given in [49].

formula [9, 50] to generate the photon spectrum. The matrix element, used by the program, for direct scalar top production is [49]:

$$\overline{|\mathcal{M}_{\gamma\gamma}|}^2 = \frac{64q^4\left[(1-\epsilon)t_{\tilde{t}}^2 u_{\tilde{t}}^2 - 2m_{\tilde{t}}^2 t_{\tilde{t}}^2 u_{\tilde{t}}^2 s + 2m_{\tilde{t}}^4 s^2\right]}{27(1-\epsilon)^2 t_{\tilde{t}}^2 u_{\tilde{t}}^2} \tag{4.1}$$

where q is the standard unit of charge, $m_{\tilde{t}}$ is the mass of the stop squark and ϵ is the polarisation vector. If the momenta of the initial photons are $k_{1,2}$ and the resultant stops are $p_{1,2}$, then the Mandelstam variables are defined as $s = (k_1 + k_2)^2$, $t_{\tilde{t}} = (k_2 - p_2)^2 - m_{\tilde{t}}^2$ and $u_{\tilde{t}} = (k_1 - p_2)^2 - m_{\tilde{t}}^2$.

It is apparent from the matrix element that the cross-section is independent of the supersymmetry breaking mechanism, as it only depends on the mass of the scalar top $m_{\tilde{t}}$. For each squark mass, the program integrates over the centre-of-mass energies and polarisations of the colliding photons, and calculates the cross-sections for direct $\gamma\gamma \to \tilde{q}\bar{\tilde{q}}$ production.

As mentioned in section 4.1.1, the photon has a hadronic structure. This implies that in addition to the direct interaction outlined above, the single- and double-resolved processes shown in figure 4.3 will also contribute to the cross-section. These are also taken into consideration during sfermion generation, and their matrix elements are [49]:

$$\overline{|\mathcal{M}_{g\gamma}|}^2 = \frac{8q^2\pi\alpha_s\left[(1-\epsilon)t_{\tilde{t}}^2u_{\tilde{t}}^2 - 2m_{\tilde{t}}^2t_{\tilde{t}}u_{\tilde{t}}s + 2m_{\tilde{t}}^4s^2\right]}{27(1-\epsilon)^2t_{\tilde{t}}^2u_{\tilde{t}}^2} \tag{4.2}$$

$$\overline{|\mathcal{M}_{q_i\bar{q}_j}|}^2 = \frac{128}{27}\delta_{ij}\pi^2\alpha_s^2\frac{t_{\tilde{t}}u_{\tilde{t}} - m_{\tilde{t}}^2s}{s^2} \tag{4.3}$$

$$\overline{|\mathcal{M}_{gg}|}^2 = \frac{\pi^2\alpha_s^2}{4(1-\epsilon)}\left[\frac{3}{8}\left(1-2\frac{t_{\tilde{t}}u_{\tilde{t}}}{s^2}\right)-\frac{8}{3}\right]\cdot\left[1-\epsilon-2\frac{sm_{\tilde{t}}^2}{t_{\tilde{t}}u_{\tilde{t}}}\left(1-\frac{sm_{\tilde{t}}^2}{t_{\tilde{t}}u_{\tilde{t}}}\right)\right] \tag{4.4}$$

where α_s is the strong coupling constant. Due to the large mass of the top quark, the terms for the t-channel contribution to $\overline{|\mathcal{M}_{q_i\bar{q}_j}|}^2$ in equation 4.3 are omitted. This is because of the negligible presence of the top quark in the photon's hadronic structure.

Cross-sections are calculated for leading order processes only, examples of which are given in figure 4.3. The leading order processes that involve the strong force, shown in figures 4.3(b, c and d), do not make a significant contribution to the cross-section in the kinematic range studied here. The main contribution to scalar top pair-production is from the direct process in figure 4.3(a). The perturbative NLO corrections for this diagram are not yet included, and are expected to be in the order of 10% [51].

The total cross-section for stop squark pair-production at the 500 GeV TESLA photon collider is shown in figure 4.4. A total of 200,000 events were generated for each squark mass, resulting in negligible errors. The figure also illustrates the effect of maximum-polarised photon beams, which are simulated with the criteria outlined in section 2.2.4. For a 180 $\mathrm{GeV/c^2}$ scalar top quark, the cross-section for unpolarised photon collisions resulting in a stop-antistop final state is $\approx 13.5\,\mathrm{fb}$.

The original program was tailored by Michael Klasen to generate weighted events for a 500 GeV photon collider. Further adjustments were performed to extract values for the transverse momentum $\left(p_T = \sqrt{p_x^2 + p_y^2}\right)$, rapidities of both stop squarks $\left(y_{1,2} = \tanh^{-1}\frac{p_{z_{1,2}}}{E_{1,2}}\right)$, and weight for each event. Momentum-Energy vectors were assigned to each stop squark with the principles discussed in Appendix A.

The program can also produce top-antitop quark pairs as a result of further amendments performed by Michael Klasen. For the kinematic range investigated,

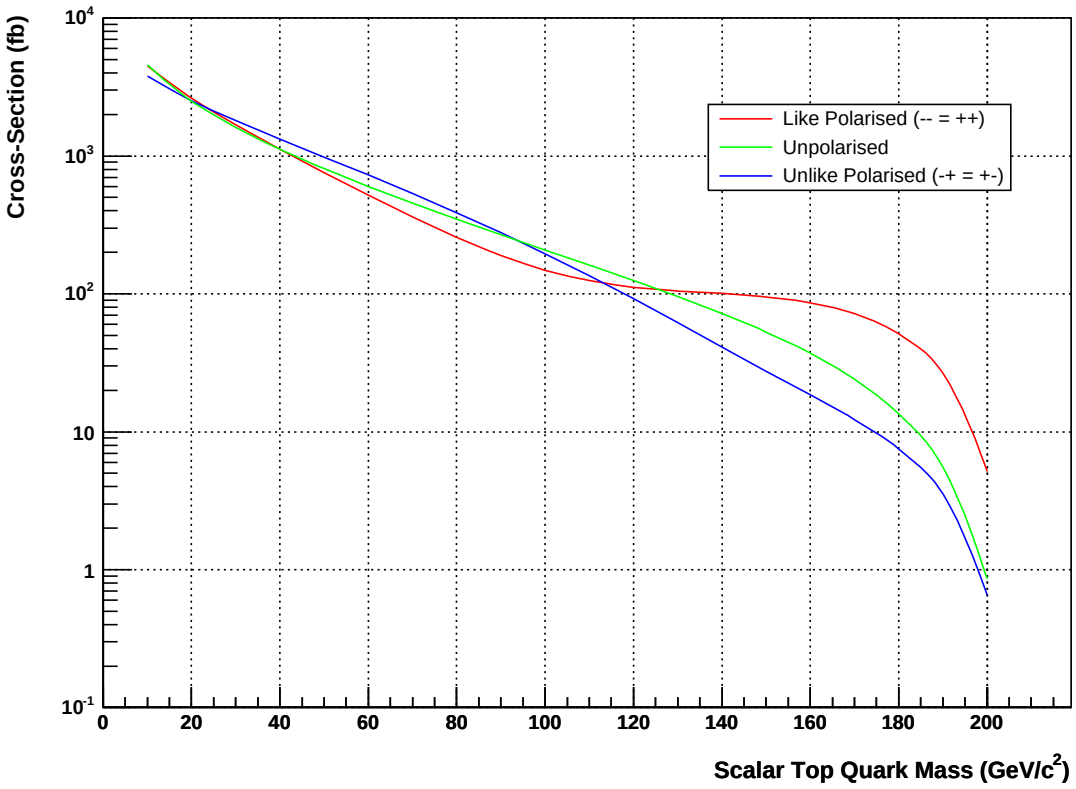

Figure 4.4: Total Cross-Section for Scalar Top Quark Production in Polarised and Unpolarised Photon-Photon Interactions at a 500 GeV Collider. Unpolarised beams are mixtures of photons with different polarisations.

Vector Meson Dominance (VMD) and anomalous couplings make a negligible contribution to the production cross-section of these particles. This is due to the large mass of the top quark. The cross-section for this background process is $\approx 58.1\,\text{fb}$.

4.1.3 Background Processes

The energy spectrums for all background processes, except top-antitop production, are generated with the CompAZ algorithm [14]. This algorithm describes the photon-energy spectrum for different electron beam energies. The photon-energy spectrum derived from the formula for simple Compton scattering differs from that observed in simulations [52]. The CompAZ routine attempts to account for these differences in the high-energy part of the spectrum.

The three processes outlined in section 2.2.3 are incorporated within the Com-

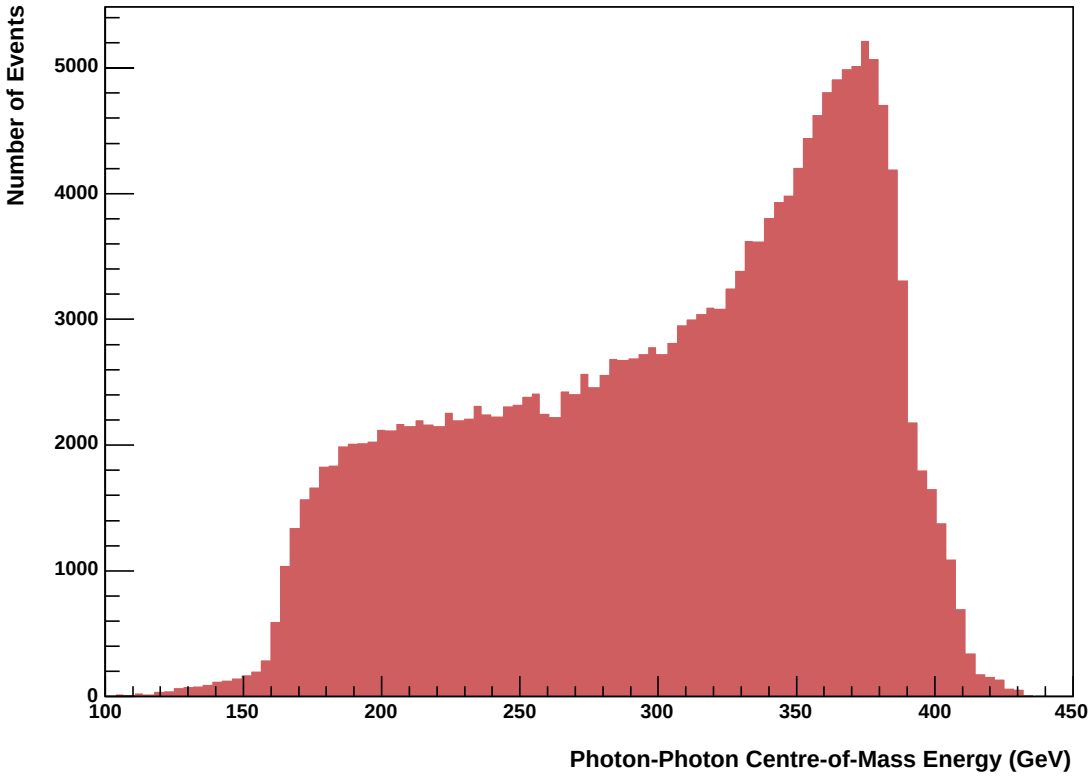

Figure 4.5: Complete Photon-Energy Spectrum for $\gamma\gamma \rightarrow W^+W^-$ Events. A total of 200,000 Events were generated with CompAZ [14] and PYTHIA 6.222 [13].

pAZ routine. The spectrum is accurately described at centre-of-mass energies $\geq 0.3\, W_{max}$ [14], where W_{max} is the maximum invariant mass of the photon system. The scalar top cannot be produced at centre-of-mass energies $< 360\,\text{GeV}$, implying that the photon-energy spectrum described by CompAZ is adequate.

For each event, two independent photons were generated within a centre-of-mass energy range of $250\,\text{GeV} \leq E_{CMS} \leq 500\,\text{GeV}$, using the CompAZGN and CompAZG2 routines. If the photons interact, a cross-section for the produced particles is calculated. Otherwise, a new pair of photons is generated, and the process is re-iterated. The complete two photon-energy spectrum for the process $\gamma\gamma \rightarrow W^+W^-$ is shown in figure 4.5.

The model that PYTHIA uses to calculate particle production cross-sections for $\gamma\gamma$ processes is described in [53], and incorporates the ideas discussed in section 4.1.1. PYTHIA calculates the cross-section σ_p by integrating over the entire photon-energy

Photon Scattering Process	Cross-Section σ (fb)			
	$\gamma\gamma \to c\bar{c}$		$\gamma\gamma \to b\bar{b}$	
	Without Cut	With Cut	Without Cut	With Cut
Direct-Direct	2670	1340	130	85
VMD-VMD	549720	10	7780	10
Anomalous-Anomalous	27840	65	3770	60
Direct-VMD	9173150	3605	116070	860
Direct-Anomalous	1069725	4100	37525	990
VMD-Anomalous	245260	50	12120	50

Table 4.1: Contributions to the Cross-Section for Heavy Quark Pair-Production. The generator-level cut on the transverse momentum of quark jets has a significant effect on the cross-section contributions from VMD and anomalous couplings.

spectrum. As the entire spectrum is not used in this analysis, CompAZG2 calculates the cross-sections within the kinematic limits expresssed above:

$$\sigma = \frac{1}{L}\int_{W_{min}}^{W_{max}} \frac{dL}{dW}\sigma_p \tag{4.5}$$

where L is the luminosity used for generation, and the minimum and maximum photon-photon centre-of-mass energies are W_{min} and W_{max} respectively.

Heavy Quark Production

Charm and beauty quarks have a similar lifetime, making it difficult to distinguish between these two particles. A $c\bar{c}$ remnant is detected from the decay of the stop squarks considered in this dissertation, indicating that charm-anticharm and beauty-antibeauty production is a source of background.

Unlike top quarks, the charm and beauty quarks are light enough to have a substantial presence in the photon's hadronic structure. As a result, interactions involving Vector Meson Dominance (VMD) and anomalous couplings have a significant contribution to the cross-section of charm and beauty pair-production. The magnitude of these contributions can be seen in table 4.1.

		$\gamma\gamma \to c\bar{c}$	$\gamma\gamma \to b\bar{b}$	$\gamma\gamma \to t\bar{t}$	$\gamma\gamma \to t\bar{t}$
Monte Carlo Generator		CompAZ	CompAZ	Klasen	CompAZ
Total Cross-Section	σ [fb]	2670	130	58	40
Events Expected	N_{events} $[10^3]$	293.7	14.3	6.5	4.4
Events Generated	N_{gen} $[10^3]$	2950	150	65	-

Table 4.2: Summary of Simulated Heavy Quark Background Events. Events were generated at photon centre-of-mass energies between 250 GeV and 500 GeV, where kinematically possible. The number of expected events was determined with an annual integrated luminosity of $110\,\text{fb}^{-1}$. Only direct-direct contributions to cross-section are shown.

Processes that involve VMD and anomalous couplings tend to be forward-peaked, which means that resultant particles from these interactions are likely to have little momentum in the transverse plane. These particles will have most of their momentum directed along the beam axis, increasing the likelihood of their escape down the beam pipe. As the detector signal for these events will consist of missing transverse momentum and energy, they potentially pose a significant background.

It is clear from table 4.1 that it is not practical to generate enough of these events to minimise errors. Therefore, a cut on the minimum transverse momentum of a quark jet can be introduced at generator-level in an attempt to mimic a similar cut at detector-level. Table 4.1 displays the results of imposing a minimum transverse momentum of 20 GeV for a charm or beauty jet.

Only direct photon-photon production of $c\bar{c}$ and $b\bar{b}$ pairs are considered in the main analysis. A separate analysis is performed for single- and double-resolved processes, with the generator-level cut in place. A summary of heavy quark pair-production from direct photon-photon collisions is given in table 4.2.

The cross-section for top-antitop production calculated by CompAZ is close to that determined by Michael Klasen's program. This implies that the generated processes are comparible, as their cross-sections are of the same order of magnitude.

Light Quark Production

Pair-production of light quarks in photon-photon interactions is heavily forward peaked at TESLA energies. The simulation of top-antitop events ignores this tendency, as the heaviest quark will be created at centre-of-mass energies close to its threshold production energy. Therefore, the top quark pair will be produced with little or no momentum. The decay of the other heavy flavours closely resembles the signature left in the detector by the signal, and therefore, cannot be ignored.

The normalised cross-section for light quark pair-production, calculated with the CompAZG2 routine, is 70 nb. This results in a total of 7.7×10^9 events in one year. Imposing an identical generator-level cut to that used for heavy quark production, from VMD and anomolous couplings, reduces the cross-section to 100 pb. A total of 12×10^6 light quark events are produced over the course of a year.

It is not practical to generate enough of these events to minimise errors, especially considering that light quark pair-production is not a major source of background for the reasons discussed above. Therefore, a small sample of 500,000 events has been generated with the generator-level cut in place. Detector-level cuts will be conducted for these events, but they will not be included in the main analysis.

W Boson Production

The reaction $\gamma\gamma \rightarrow \mathrm{W}^+\mathrm{W}^-$ is a golden channel process at the TESLA photon collider [6]. The cross-section for this interaction, as adjusted by the CompAZG2 routine, is $\approx 15\,\mathrm{pb}$.

There are two possible decay processes for a $\mathrm{W}^\pm$ boson. A $\mathrm{W}^\pm$ boson is said to have decayed leptonically if it decays to a lepton-neutrino pair of the same generation. A $\mathrm{W}^\pm$ boson decays hadronically to a quark-antiquark pair $\mathrm{q}_i\bar{\mathrm{q}}_j$, where q_i and $\bar{\mathrm{q}}_j$ are different flavoured quarks of the same generation.

The contribution to background made by both $\mathrm{W}^\pm$ bosons decaying leptonically or hadronically can be reduced by imposing certain detector-level cuts. However, signatures left by one leptonic and one hadronic decay can be a source of irreducible

		$\gamma\gamma \rightarrow W^+W^- \rightarrow$		
		$q_i\bar{q}_j q_k\bar{q}_l$ (Hadronic)	$q_i\bar{q}l\nu$ (Mixed)	$l\nu l\nu$ (Leptonic)
Total Cross-Section	σ [fb]	6390	6650	1530
Events Expected per Year	N_{events} [10^3]	731.5	702.9	168.3
Events Generated	N_{gen} [10^3]	7320	7175	-

Table 4.3: Summary of simulated W^+W^- Background Events. Events were generated at photon centre-of-mass energies between 250 GeV and 500 GeV, and the number of expected events was determined with an integrated luminosity of $110\,fb^{-1}$.

background. A W^+W^- pair producing a $q_i\bar{q}_j l\nu$ final state will leave a signature of two quark jets, one lepton and missing energy in the detector. This is similar to the detector response for stop decays, and it becomes difficult to differentiate between these two signals when either a c or b quark is produced.

A summary of W^+W^- production in photon-photon collisions is given in table 4.3. Events where both $W^{\pm}$ bosons decay leptonically do not make a contribution to the background, and therefore have been excluded in this analysis.

4.1.4 Z Boson Production

Direct photon-photon interactions do not create neutral bosons, such as the Z^0. In fact, the probability of a Z^0 boson coupling to two photons is $< 5.2 \times 10^{-5}$ [18].

However, two Z^0 bosons can be produced in second-order processes [54], such as those shown in figure 4.6. Single Z^0 resonance production, which is shown in figure 4.6(d), has been considered in quark-antiquark production. The processes illustrated in figure 4.6(a, b and c) are of higher order, and therefore have small production cross-sections.

The total cross-section for these second order processes is $\approx 30\,fb$ [54], which has been integrated over the entire photon-energy spectrum. Using an optimistic integrated luminosity of $110\,fb^{-1}$, approximately 3300 $\gamma\gamma \rightarrow Z^0Z^0$ events occur in

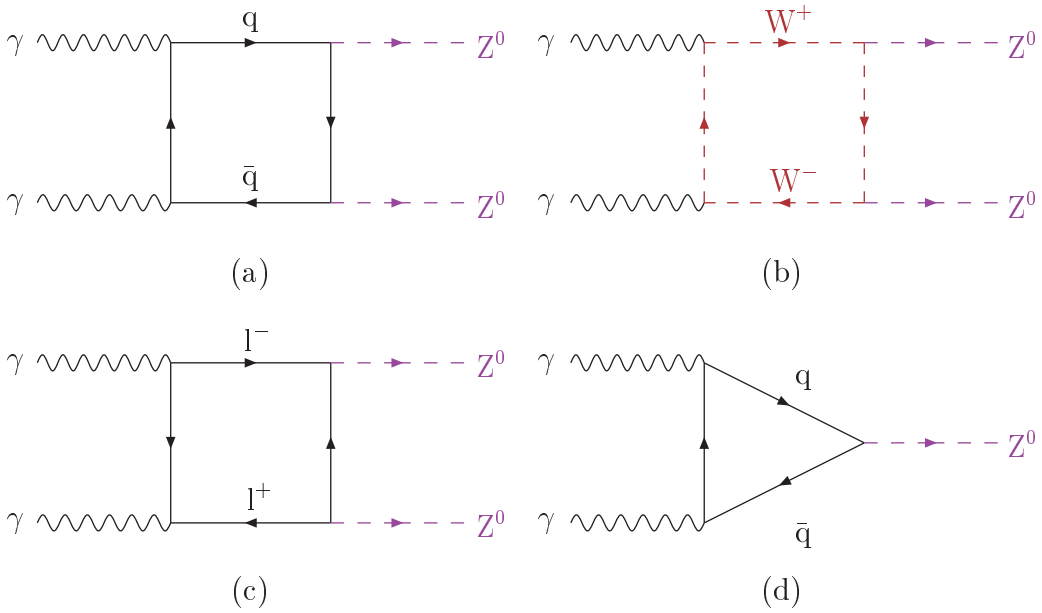

Figure 4.6: Feynman Diagrams illustrating Z^0 Boson Production at a Photon Collider: (a) $\gamma\gamma \to q\bar{q} \to Z^0Z^0$; (b) $\gamma\gamma \to W^+W^- \to Z^0Z^0$; (c) $\gamma\gamma \to l^+l^- \to Z^0Z^0$; and (d) $\gamma\gamma \to q\bar{q} \to Z^0$. A complete set of Feynman diagrams is given in [54]. The purple and maroon coloured dashed lines represent Z^0 and $W^\pm$ bosons respectively.

one year.

With PYTHIA, 10% of these pairs will both decay leptonically, and therefore are not background events. Assuming the photon-energy spectrum for Z^0 boson pair-production is similar to that for $\gamma\gamma \to W^+W^-$ events, which is shown in figure 4.5, around $\frac{1}{3}$ of these events will not occur when $E_{CMS} > 250\,\text{GeV}$. This leaves a total of 1,980 hadronic and semi-leptonic decays. This number is small enough with respect to W^+W^- production to justifiably exclude these events from this analysis.

4.1.5 Electron-Electron and Photon-Electron Interactions

The beam which arrives at the second interaction point will comprise of a mixture of photons and electrons, as discussed in section 2.2.2. As a result, photon-electron and electron-electron collisions can occur. The probability of electron to photon conversion is estimated to be 63% [6]. Therefore, there will be a significant number of electrons arriving at the interaction point.

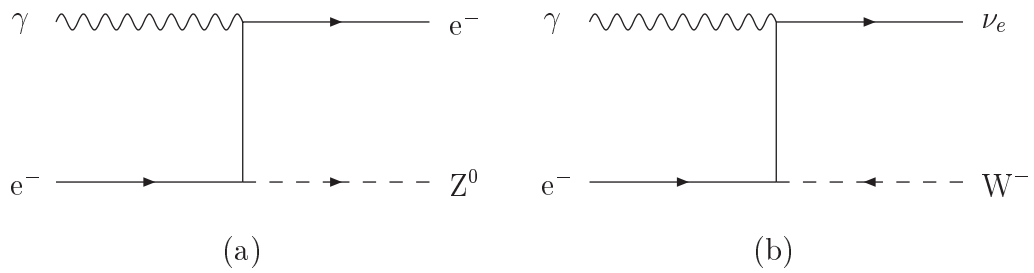

Figure 4.7: Feynman Diagrams illustrating Possible Gauge Boson Production in Photon-Electron Interactions: (a) $\gamma e^- \rightarrow Z^0 e^-$; and (b) $\gamma e^- \rightarrow W^- \nu_e$

Electron-electron collisions can result in electron-electron and selectron-selectron pair-production, where the selectron is the superpartner of the electron. The centre-of-mass energies for these collisions is similar to that present in electron-positron interactions. These processes will not contribute to the background, and can be safely neglected.

Photon-Electron interactions, however, can produce a multitude of different particles. Feynman diagrams for two possible backgrounds are shown in figure 4.7. The high-energy luminosity of photon-electron collisions at the 500 GeV TESLA photon collider is $94\,\mathrm{fb}^{-1}$ [6], which is slightly lower than that for $\gamma\gamma$ interactions. This reduction is partly due to beamstrahlung effects and photoproduction of e^+e^- pairs. However, backgrounds from photon-electron collisions are still substantial, and should be considered in a complete analysis. These effects are not considered in this dissertation.

4.2 Particle Fragmentation

The Monte Carlo program PYTHIA [13] is used to decay all generated particles. The CompAZGN and CompAZG2 routines have been specifically designed to provide an interface with PYTHIA, thus allowing the fast generation and fragmentation of most background events. In contrast, the momentum-energy vectors for stop and top particles are externally fed into PYTHIA.

4.2.1 Quark Decay

The hadronisation process, which is described in section 3.1.4, is not as yet fully understood. There are a number of different frameworks available for the production of jets from isolated quarks, of which PYTHIA uses the Lund String Model [55].

In a typical $\gamma\gamma \rightarrow q\bar{q}$ event, the quark and antiquark are connected together by a set of gluons. This structure is known as a string, and its fragmentation is dependent on its mass. A detailed explanation of the hadronisation process for charm and beauty quarks is given by [56].

Branching ratios for the decays of resultant hadrons are obtained from current experimental values, due to the difficulty in deriving these from first principles. The probability that a particle will decay into a final state is the branching ratio for that decay.

4.2.2 Gauge Boson Decay

Unlike most quarks, branching ratios for the decays of gauge bosons are calculated from perturbation theory [13]. In the context of this work, the $W^{\pm}$ and Z^0 particles are treated in this manner. In addition, the top quark is also regarded as a resonance by PYTHIA, but predominantly decays to a bW^+ state.

4.2.3 Scalar Top Decay

Like most supersymmetric particles, the branching ratios for stop squarks are calculated from perturbation theory, similar to that used for resonance decay. However, as discussed in section 3.4.3, the decay chain for the scalar top quark is also reliant upon certain parameters of the MSSM (Minimal Supersymmetric Standard Model). Branching ratios, as a function of the SU(2) gaugino mass parameter, for $\tilde{t}_1$ decay are shown in figure 4.8.

Values of the MSSM parameters used in the program for scalar top quark decay are given in table 4.4. Masses of $180\,\mathrm{GeV/c^2}$ for the stop squark and $100\,\mathrm{GeV/c^2}$

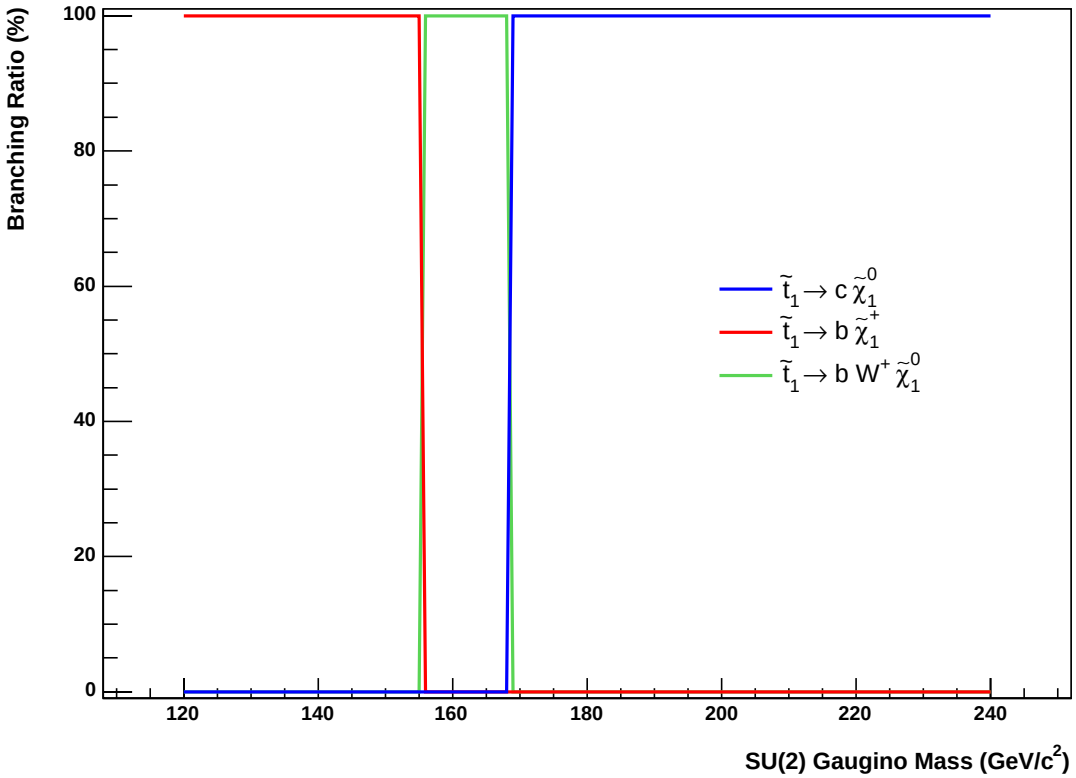

Figure 4.8: Branching Ratios for Scalar Top Quark Decay as a function of the SU(2) Gaugino Mass MSSM Parameter. The graph is drawn for $m_{\tilde{t}_1} = 180$ GeV/c^2, $\cos\theta_{\tilde{t}} = 0.7$, $\tan\beta = 2$, and $\mu = -500$ GeV/c^2. Values for the branching ratios were extracted from PYTHIA, and can be compared with similar results in [41].

MSSM Parameter	Symbol	Value	Units
U(1) gaugino mass	M_1	97.75	GeV
SU(2) gaugino mass	M_2	211	GeV
Higgsino mass	μ	-500	GeV
Ratio of Higgs expectation values	$\tan\beta$	2	
Scalar top mass	$m_{\tilde{t}_1}$	180	GeV
Scalar top mixing angle	$\cos\theta_{\tilde{t}}$	0.7	rad.

Table 4.4: Values of Supersymmetry Parameters set for Stop Squark Decay. The channel $\tilde{t}_1 \to c\tilde{\chi}_1^0$ has a 100% branching ratio when these parameters are used.

for the first mass eigenstate of the neutralino emerge from these values. The U(1) gaugino mass has a strong effect on $m_{\tilde{\chi}_1^0}$.

In contrast, the lighter mass eigenstate of the chargino is affected by the SU(2) gaugino mass parameter (M_2). The magnitude of this can be seen from the equation for the mass of the $\tilde{\chi}_1^{\pm}$ [23]:

$$m^2_{\tilde{\chi}_1^{\pm}} = \frac{1}{2}\left(M_2 + \mu^2 + 2M^2_{W^{\pm}}\right) - \frac{1}{2}\left(\sqrt{\left(M_2^2 + \mu^2 + 2M^2_{W^{\pm}}\right)^2 - 4\left(\mu M_2 - M^2_{W^{\pm}} \sin 2\beta\right)^2}\right) \quad (4.6)$$

where $M_{W^{\pm}}$ is the mass of the W boson. When the parameters shown in table 4.4 are set, the mass of the $\tilde{\chi}_1^{\pm}$ is $\approx 217\,\mathrm{GeV/c^2}$. Therefore, the beauty-chargino and beauty-neutralino-W boson decay channels mentioned in section 3.4.3 are not kinematically possible. As a result, the decay $\tilde{\mathrm{t}}_1 \rightarrow \mathrm{c}\tilde{\chi}_1^0$ has a 100% branching ratio.

Chapter 5

Event Selection and Analysis

5.1 Particle Detection

Decay records for all events were passed to the fast TESLA detector simulation program Simdet 4.0.3 [57], in an attempt to mimic the response of the detector. Resolution functions for particle momenta and charge, impact parameters, and calorimeter energies are provided by the Monte Carlo program program BRAHMS [58]. This information is used by Simdet to construct a realistic model for particle detection at TESLA.

Simdet selects stable particles from the decay record, and smears their properties with Gaussian fits defined by the detector resolution functions. Weakly interacting stable particles, such as the neutralino and neutrinos, are not included. Additionally, stable particles that escape down the beam pipe are also rejected. The remaining photons, electrons, muons and hadrons must satisfy the minimum energy requirements given in table 5.1, which reflect the finite resolution of the detector. A comparison between invariant mass distributions before and after smearing can be seen in figure 5.1. It is evident from this figure that the magnitude of smearing is relatively small.

A summary of available parameters for detector resolution and response in Simdet is given in table 5.1. Particles that do not satisfy the minimum values

Tracking System		
Track measurement efficiency	100	%
Minimum transverse energy for detector response	0.10	GeV
Probability of charge misidentification	0.50	%
Electromagnetic Calorimeter		
Minimum energy for photon detection	0.20	GeV
Probability of electron misidentification	0.20	%
First energy resolution parameter	0.145	
Second energy resolution parameter	0.015	
Hadronic Calorimeter		
Minimum energy for hadron detection	0.50	GeV
First energy resolution parameter	0.554	
Second energy resolution parameter	0.166	
Muon Detector		
Average Muon energy deposited in calorimeters	3.80	GeV
Minimum energy for isolated muons	5.00	GeV
Probability of muon misidentification	0.50	%
Low Angle Tagger		
Minimum energy for particle detection	5.00	GeV
First energy resolution parameter	0.100	
Second energy resolution parameter	0.010	
Polar angle resolution	0.040	rad.
Azimuthal angle resolution	0.262	rad.

Table 5.1: Values of the Simdet Parameters that determine Detector Resolution and Response. The resolution parameters are the result of the parametrisation of resolution functions from BRAHMS [58]. All events are analysed by the Simdet detector simulation using these constants. The effects of these values are discussed in further detail by [57].

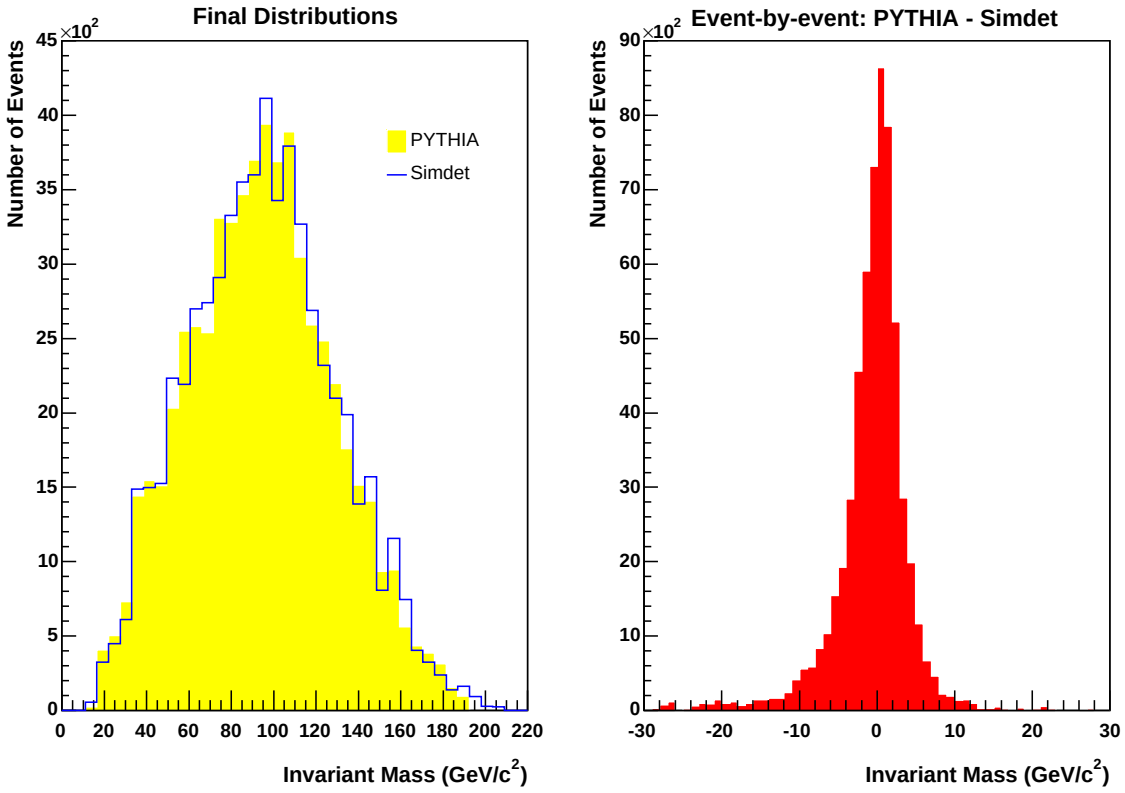

Figure 5.1: Comparison of Invariant Mass Distributions from PYTHIA and Simdet for $\tilde{t}_1 \rightarrow c\tilde{\chi}_1^0$ Events. The final invariant mass distributions (left plot) and the event-by-event difference between the invariant masses from PYTHIA and Simdet (right plot) are displayed. Only stable particles that cause a response in the detector are shown. A total of 60,000 events were generated.

of table 5.1 will not be detected. The CCD technology option, which is outlined in section 2.3.1, is simulated for the microvertex detector. All charged particles with a transverse momentum above 0.1 GeV will create a track. Electric charges for tracks with a high transverse energy have a 0.5% probability of being misidentified, which increases to 1.5% for badly reconstructed tracks.

The SiW and the tile options for the electromagnetic (section 2.3.2) and hadronic (section 2.3.3) calorimeters respectively are implemented by Simdet. Due to the lack of tracking in front of the low angle tagger (section 2.3.5), electrons, positrons and photons detected at this calorimeter cannot be distinguished from each other. As a result, they are all treated as photons by Simdet.

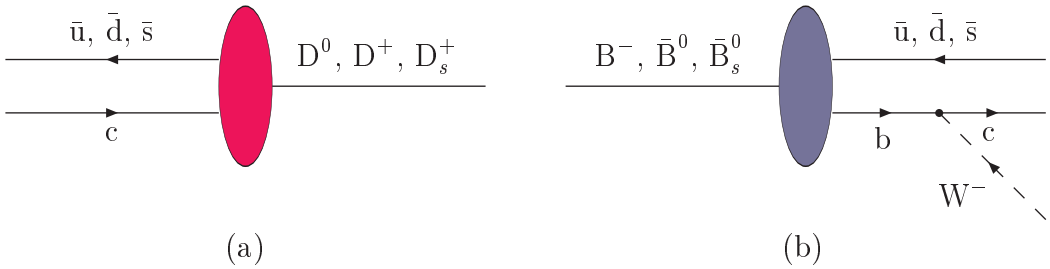

Figure 5.2: Diagrams illustrating: (a) D-Meson Production; and (b) B-Meson Decays. An virtual W boson is emitted in B-meson decay, which decays rapidly to produce leptons or hadrons.

After an event has been passed through the Simdet machinery, the properties of detected particles are written to a file. The structure of this output file is described by [57].

5.2 Event Reconstruction

The tracks made by heavy quark decay can be used to determine the flavour of their parent particle. This process is known as flavour tagging, and its accuracy depends on the resolution of the tracking system. Due to the high luminosities available at next generation colliders, quark tagging will play an important role.

Signal decays result in the creation of charm quarks, which have a mass that lies between that for strange and beauty quarks. Unlike the fragmentation of light quarks, jets formed from charm quarks often contain a high energy D-meson. In contrast, the hadronisation of beauty quarks normally results in a B-meson. The characteristics between these two processes are illustrated in figure 5.2. In figure 5.2(a) a charm quark forms a D-meson by being combined with an antiquark. Figure 5.2(b) indicates that a D-meson can be produced from B-meson decay by the confinement of the charm quark with a light antiquark.

A D-meson from B-meson decay will have a lower momentum than one from the fragmentation of a primary charm quark. Additionally, an extra vertex will be present, which will show evidence of beauty, rather than charm, quark production.

Charm quarks can also be identified by looking for exclusive D-meson decay modes, such as $D^0 \rightarrow K^- \pi^+$.

The ZVTOP [59] vertex algorithm was designed by the Stanford Large Detector (SLD) Collaboration. It attempts to reconstruct quark jets using the tracks and displaced vertices left behind by an event. This algorithm has been amended to facilitate the inclusion of a neural network [60]. Events that include quark-antiquark production can be used to train a neural network, which learns how to distinguish the different resultant particles.

An interface [60] between Simdet and the ZVTOP vertex finder is used to extract information collected by the CCD detector. The neural network supplied by Thorsten Kuhl for beauty and charm tagging has been trained on high-energy $e^+e^- \rightarrow H^0Z^0 \rightarrow l^+l^-q\bar{q}$ events. Over 300,000 events [61] for every possible decay mode were used to train the neural network.

Probabilities of the presence of beauty and charm quarks are given in relation to light quarks. Additionally, the likelihood of charm quark production is also compared with that for beauty quarks. The Simdet code was altered, thus enabling these tagging probabilities to be written on the standard output file.

5.3 Event Properties

A program for reading data from the Simdet standard output file has been designed. The computer program collects momentum-energy vectors for detected particles, and calculates the invariant mass, transverse momentum, multiplicity and energy for each event.

The ZVTOP [59] algorithm calculates the thrust, thrust angle and, together with the neural network [60], tagging probabilities of an event. The algorithm also determines the number of vertices produced by a quark jet. The aforementioned program extracts these values from the standard output file.

An additional program calculates the transverse energy within cones surrounding

an electron or muon. This is done in an attempt to distinguish isolated leptons from those that form part of a quark jet.

5.4 Background Reduction

A variety of cuts are performed on the collected data in an effort to maximise the signal-to-background ratio. The changes in invariant mass and energy distributions as cuts are applied are illustrated in figures 5.5 and 5.6 respectively. A large missing energy, as evidence for the signal, is expected owing to the production of two neutralinos. This should be clear from the chosen distributions. Details of these cuts are explained below.

5.4.1 Thrust Angle

Thrust is a dimensionless quantity that attempts to reconstruct the position in phase space of the original particles from their decay products. It is defined as:

$$T = \max_{|\hat{n}|=1} \frac{\sum_i |\hat{n} \cdot \vec{p}_i|}{\sum_i |\vec{p}_i|} \tag{5.1}$$

where $\vec{p}_i$ is the momentum vector for each detected particle. The thrust axis is given by the unit vector $\hat{n}$, which maximises the value given by equation 5.1. The thrust axis gives an indication of the sphericity of the event, and its polar angle can be used to illustrate the direction of particle production. This quantity is known as the thrust angle.

Events in which some particles escape down the beam pipe will have a thrust angle close to the z-axis. As a result, these events will leave a large amount of missing energy within the detector. As missing energy is expected from scalar top decay, background events that follow this pattern can be confused with the signal. In an effort to exclude these events, a thust angle cut of $-0.7 < \cos\theta_{Thrust} < 0.7$ is performed.

The cut also has the added benefit of removing a large amount of background events relative to the signal. This can be seen from the thrust angle distributions

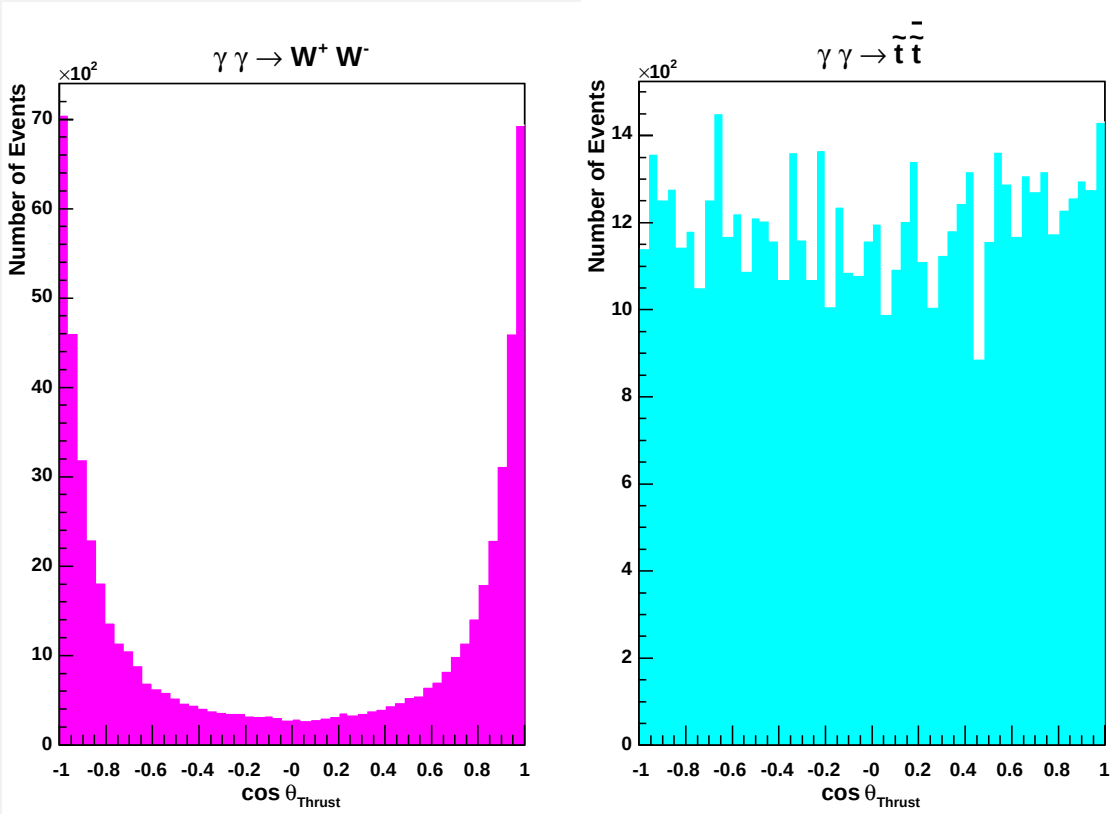

Figure 5.3: Comparison between Thrust Angle Distributions for W^+W^- (left plot) and $\tilde{t}\bar{\tilde{t}}$ (right plot) Events.

in figure 5.3. As the stop squark is a scalar particle, it does not have a preferential direction of production. This can be compared with vector particles, such as $W^{\pm}$ boson production, which is heavily forward-peaked.

The results of this cut can be seen in figures 5.5 and 5.6. The low-energy peak of quark-antiquark background, which represents events where some particles have escaped down the beam pipe, has been eliminated. The cut has a relatively small effect on top-antitop prodcution, as the photon-photon invariant mass required to create these particles is close to the threshold production energy.

5.4.2 Missing Transverse Momentum

A requirement of a minimum momentum of 20 GeV in the transverse plane has been applied to remove events that do not possess any missing energy. As transverse momentum is conserved in every interaction, events where all particles are detected

have $p_T = 0$. The cut leads to a relatively large reduction in quark-antiquark and hadronic W^+W^- backgrounds. However, there is no significant reduction of $W^+W^- \to q_i\bar{q}_j l\nu$ events. Figures 5.5 and 5.6 show that this is the main background process.

5.4.3 Multiplicity

Events with less than 25 detected particles were excluded from this analysis. This cut, although minimal in its effectiveness, is important for several reasons. To increase the effectiveness of any further cuts, events with a relatively high multiplicity are desirable. In addition, any stray leptonic events are eliminated after this cut.

5.4.4 Isolated Lepton

Although a significant reduction of the $W^+W^- \to q_i\bar{q}_j l\nu$ background is achieved using the cuts outlined above, it still engulfs the signal. As discussed in section 4.1.3, this background can be reduced by searching for leptons that do not form part of a jet. Channels that result in tau-lepton production are not affected as this lepton decays before reaching the detector.

The position of particles within the detector can be expressed in the η-ϕ plane, where ϕ is the azimuthal angle. The pseudorapidity is a Lorentz invariant quantity for massless particles, and is defined as:

$$\eta = -\ln \tan\left(\frac{\theta}{2}\right) \tag{5.2}$$

where θ is the polar angle. Distances on this plane are given by:

$$R = \sqrt{(\Delta\eta)^2 + (\Delta\phi)^2} \tag{5.3}$$

Leptons that form part of a quark jet will have a cluster of other particles surrounding them. This is in contrast with isolated leptons, which should have little or no particles within a certain radius. A circle drawn around leptons in the η-ϕ plane is used to represent a cone, originating from the point of production. The presence

Transverse	Radius = 0.5			Radius = 0.7		
Energy	Efficiency (%)		S/B	Efficiency (%)		S/B
(GeV)	W^+W^-	$\tilde{t}\bar{\tilde{t}}$	Ratio $[10^{-3}]$	W^+W^-	$\tilde{t}\bar{\tilde{t}}$	Ratio $[10^{-3}]$
No Cut	100	100	5.4	100	100	5.4
> 10	67	98	7.9	70	99	7.6
> 15	66	98	8.0	69	98	7.7
> 20	65	97	8.0	68	98	7.7
> 25	64	95	8.0	67	96	7.7
> 30	63	93	7.9	66	95	7.7

Table 5.2: Cut Efficiencies and Signal-to-Background Ratios for Isolated Electron Cut. Signal-to-background ratios are given with respect to $W^+W^- \rightarrow q_i\bar{q}_j l\nu$ events only.

of other particles within this cone indicates that the lepton is part of a quark jet. The reverse is true for isolated electrons and muons.

However, the situation is made slightly more complicated by detector issues. For example, a damaged detector plate may respond to an imaginary particle, thus incorrectly indicating that an isolated lepton is part of a quark jet. In an attempt to eliminate these incidents, a limit on the sum of transverse energies for all particles within this cone is defined. Below this limit, the lepton is isolated, and can be eliminated from this analysis.

Electrons and muons are analysed seperately, and radii of 0.5 and 0.7 have been chosen. Details on the effect of this cut for varying values of minimum transverse energy for electrons and muons are detailed in tables 5.2 and 5.3 respectively. A minimum value of 20 GeV for the transverse energy within a cone of radius 0.5 has been chosen to symbolise an electron or muon that is part of a quark jet.

The effect of this cut can be seen in figures 5.5 and 5.6. This cut successfully removes a large number of $W^+W^- \rightarrow q_i\bar{q}_j l\nu$ events, and has a strong effect on the top-antitop background. Efficiencies of 64% and 60% for the isolated electron and muon cuts respectively are achieved for the $t\bar{t}$ background. This is because a top

Transverse	Radius = 0.5			Radius = 0.7		
Energy	Efficiency (%)		S/B	Efficiency (%)		S/B
(GeV)	W^+W^-	$\tilde{t}\bar{\tilde{t}}$	Ratio $[10^{-2}]$	W^+W^-	$\tilde{t}\bar{\tilde{t}}$	Ratio $[10^{-2}]$
No Cut	100	100	0.8	100	100	0.804
> 10	50	98	1.6	55	99	1.5
> 15	49	98	1.6	53	98	1.5
> 20	48	97	1.6	52	98	1.5
> 25	48	96	1.6	51	96	1.5
> 30	47	94	1.6	51	95	1.5

Table 5.3: Cut Efficiencies and Signal-to-Background Ratios for Isolated Muon Cut. Signal-to-background ratios are given with respect to $W^+W^- \to q_i\bar{q}_j l\nu$ events only. Analysis was performed after isolated electron cut.

quark will decay to a W^+b state, where the W boson could decay leptonically. As expected, the cut has little effect on other backgrounds.

5.4.5 Number of Vertices

The number of vertices left in the tracker is dependent on the original quark flavour, and this property can be used to remove some light quark events. Histograms illustrating the number of vertices produced by signal and $W^+W^- \to q_i\bar{q}_j l\nu$ events are shown in figure 5.4.

As expected, roughly equal numbers of charm quark jets result in one or two vertices. Most jets that originate from light quarks leave a signature of one vertex in the tracking system. A cut of 2 vertices on the most energetic jet eliminates a large amount of hadronic and mixed W^+W^- events relative to the signal. A further identical cut on the second most energetic jet yields similar results. A signal efficiency of 43% and 37% is achieved by the cuts on the leading and sub-leading jets respectively. This compares well with a respective $W^+W^- \to q_i\bar{q}_j l\nu$ background efficiency of 13% and 10%. The results of these cuts are illustrated in figures 5.5

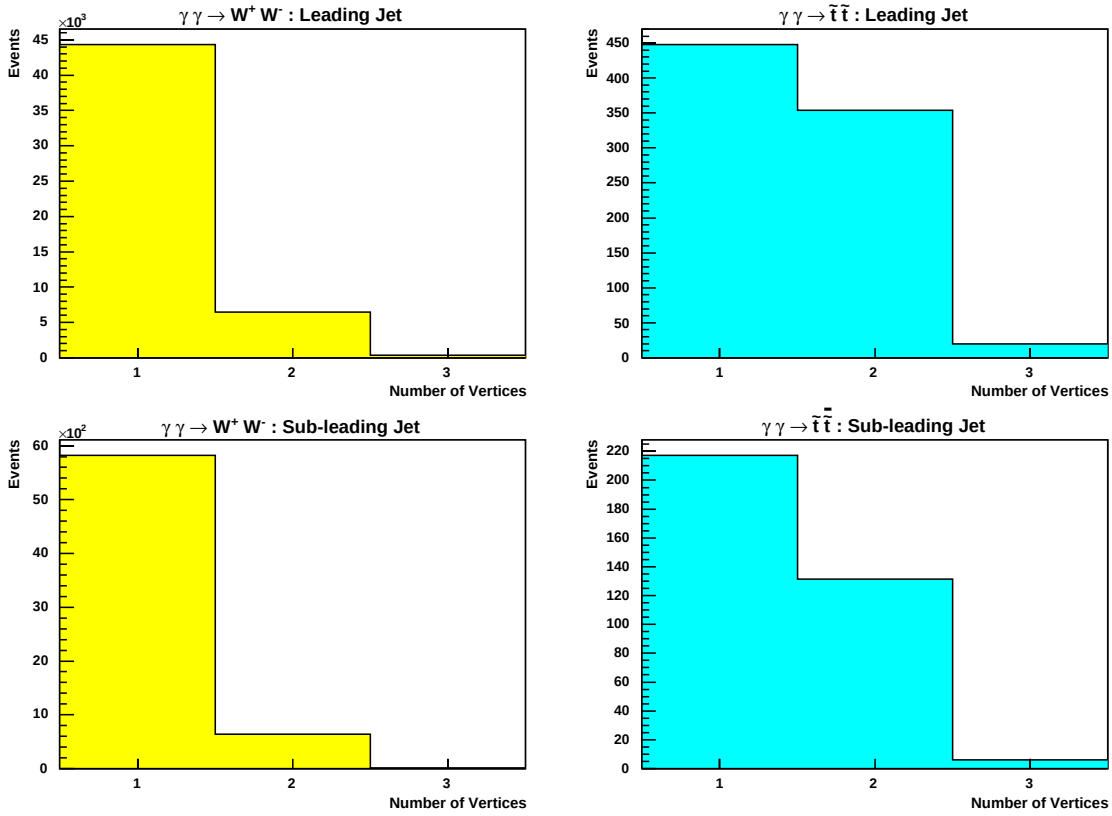

Figure 5.4: Distributions of Number of Vertices Produced by Quark Jets from $W^+W^- \rightarrow q_i\bar{q}_j l\nu$ and Signal Events. Distributions for sub-leading jets are taken after the implementation of a cut on the number of vertices for the leading jet.

and 5.6.

5.4.6 Charm Tagging

In an effort to search for evidence of charm quarks, cuts can be imposed on the jet tagging variables described in section 5.2. The network outputs a charm quark probability for the two most energetic jets in relation to light and beauty quarks.

The probability distributions for c quark events with respect to light quarks is shown in figure 5.7. The histograms are filled after the vertex cut is performed on the data. As expected, beauty quarks from $\gamma\gamma \rightarrow b\bar{b}$ and $\gamma\gamma \rightarrow t\bar{t}$ events are mostly classified as charm quarks, owing to the similarity in mass of c and b quarks. However, a relatively large number of c quarks from $\gamma\gamma \rightarrow c\bar{c}$ events possess a low charm tag probability. Applying a minimum cut of 0.1 to this property for both

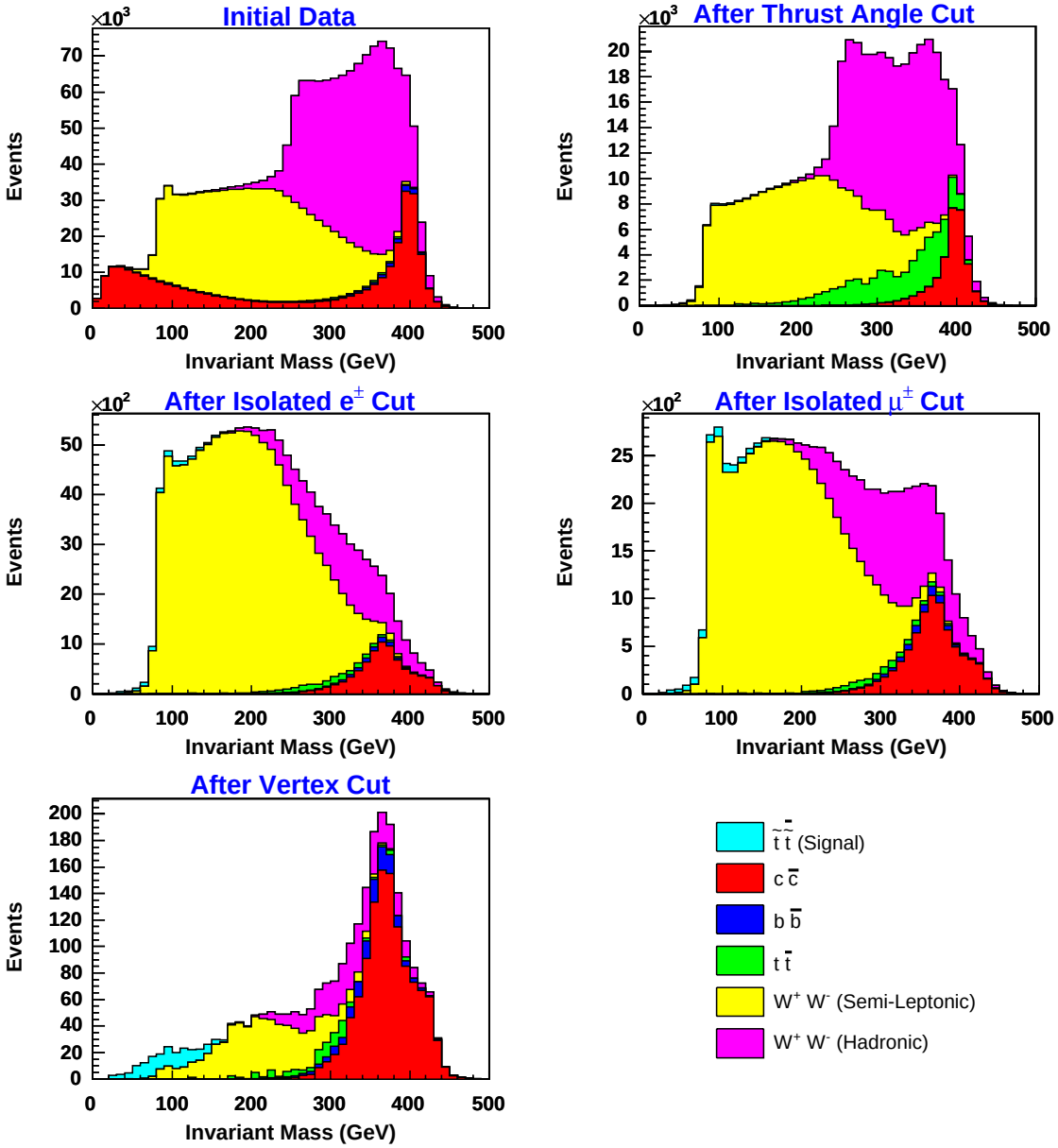

Figure 5.5: Evolution of Invariant Mass Distributions for Signal and Background Events. In the order that they are applied: before cuts; after thrust angle cut; after isolated electron cut; after isolated muon cut; and after vertex cut.

leading and sub-leading jets leads to an increase in the signal to mixed W^+W^- background ratio. This cut provides $c\bar{c}$, $W^+W^- \rightarrow q_i\bar{q}_j l\nu$ and signal efficiencies of 10%, 31% and 53% respectively.

Charm probability distributions compared with beauty quarks are shown in fig-

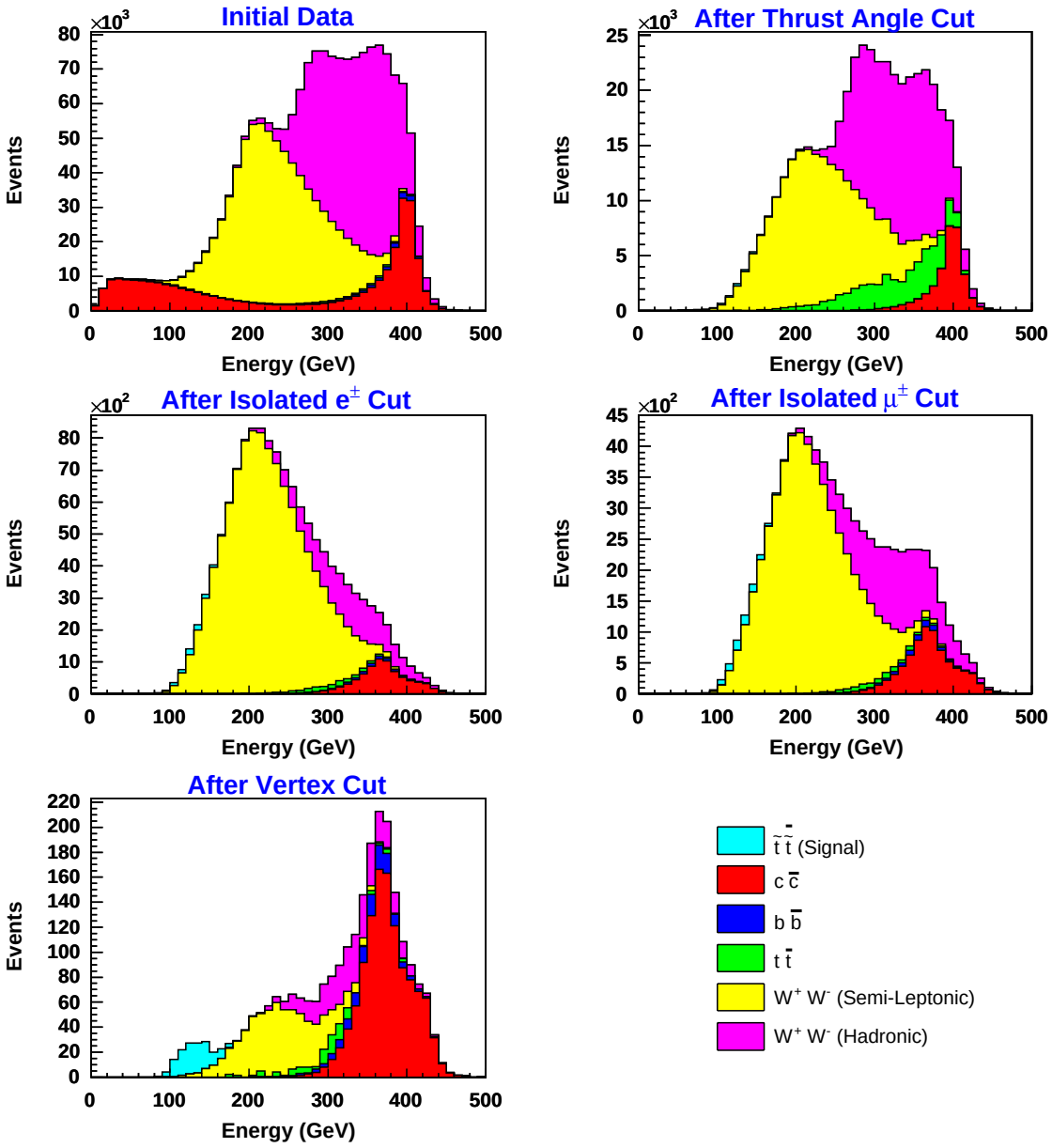

Figure 5.6: Evolution of Energy Distributions for Signal and Background Events. In the order that they are applied: before cuts; after thrust angle cut; after isolated electron cut; after isolated muon cut; and after vertex cut.

ure 5.8. Implementing a minimum cut of 0.1 for leading and sub-leading jets rejects a significant number of $\gamma\gamma \to b\bar{b}$ and $\gamma\gamma \to t\bar{t}$ events. Relatively large $c\bar{c}$ and signal efficiencies of 79% and 91% are achieved. The cut also renders an efficiency of 83% for the main background, $W^+W^- \to q_i\bar{q}_j l\nu$ decay, thus resulting in an improved

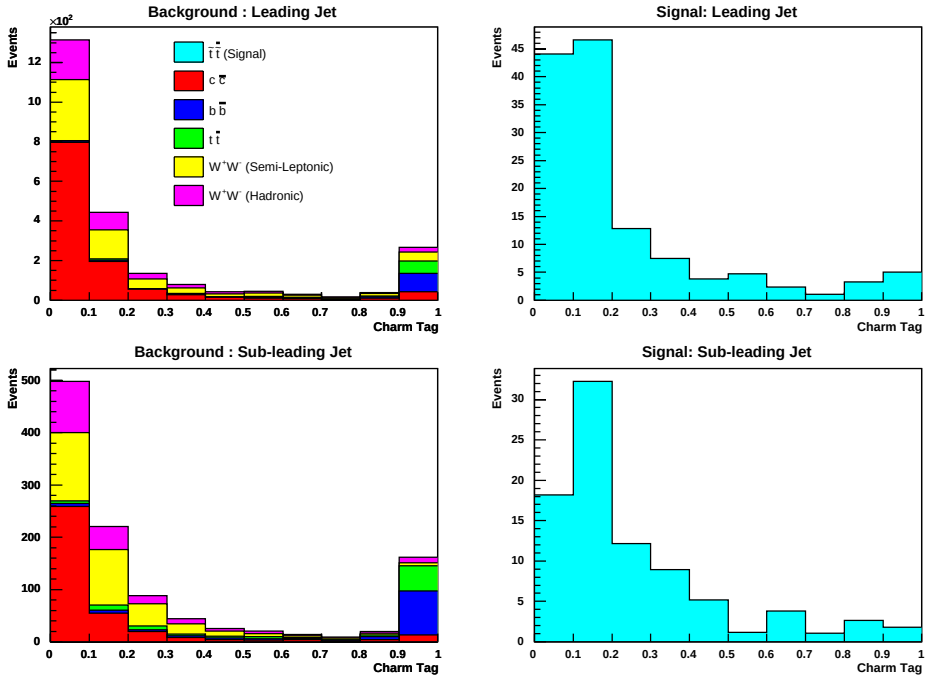

Figure 5.7: Distributions for Output from Neural Network trained to discern Charm Jets from Light Quarks. Data for sub-leading jets are taken after a cut has been implemented on the leading jet.

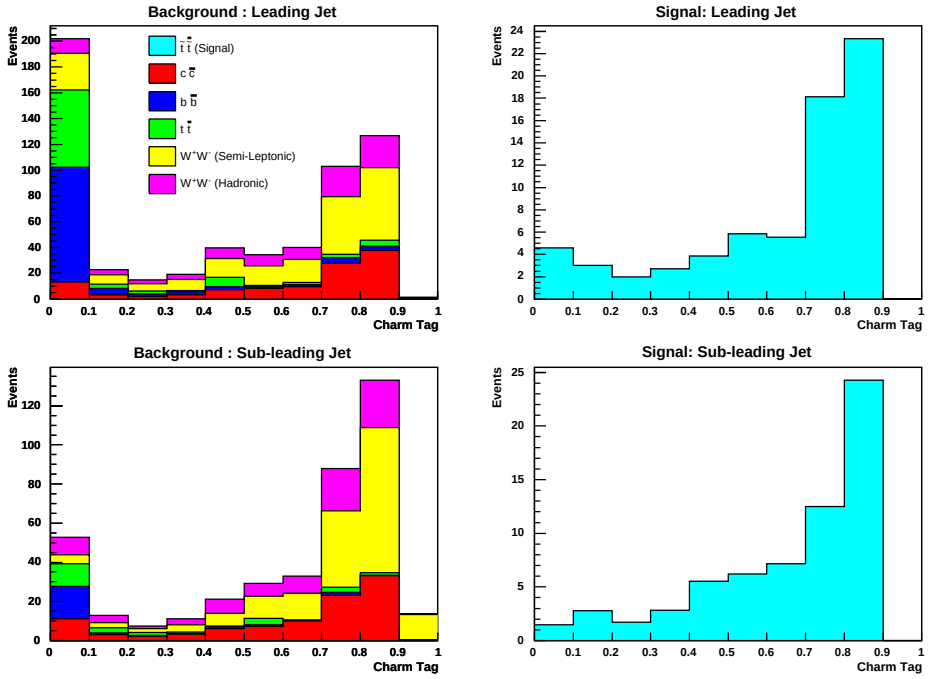

Figure 5.8: Distributions for Output from Neural Network trained to discern Charm Jets from Beauty Quarks. Data for sub-leading jets are taken after a cut has been implemented on the leading jet.

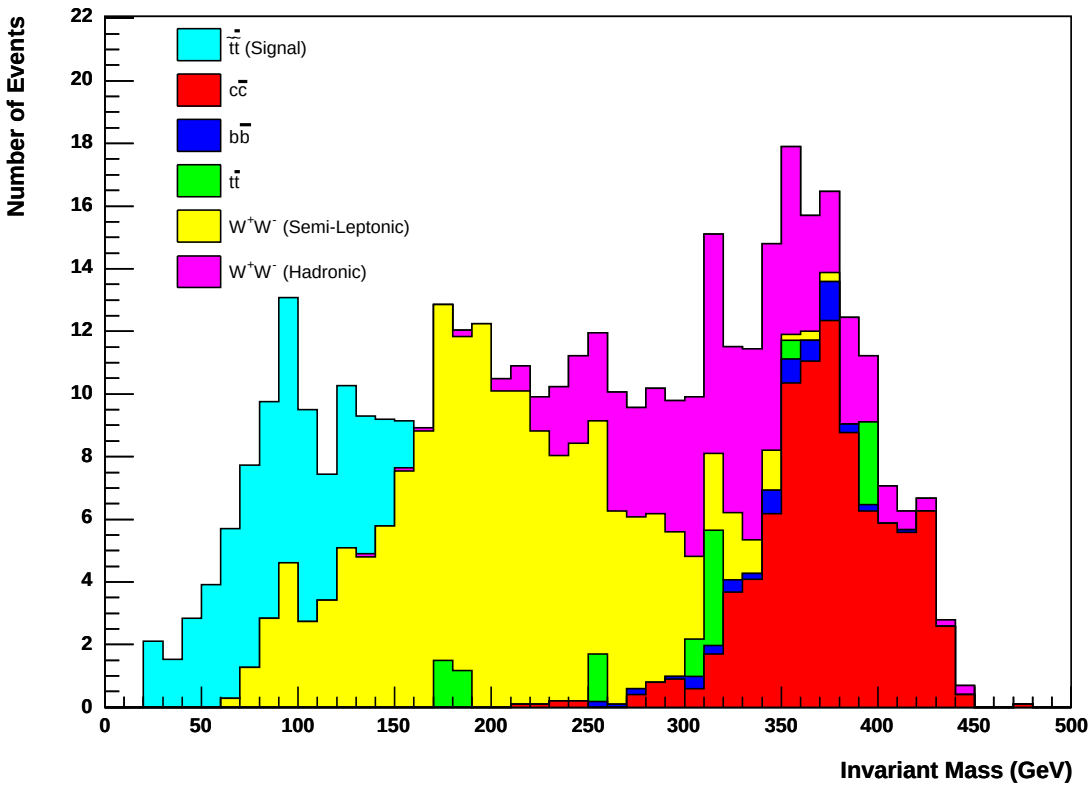

Figure 5.9: Invariant Mass Distributions for Signal and Background Events after all cuts have been applied.

signal-to-background ratio.

5.5 Analysis

Invariant mass and energy histograms for background and signal events after all cuts are shown in figures 5.9 and 5.10 respectively. Both sets of histograms show the presence of three peaks. For figure 5.9 these peaks occur at approximately 90 GeV, 180 GeV and 360 GeV for scalar top, semi-leptonic W^+W^- and hadronic events respectively. In figure 5.10 the peaks have similar values of 120 GeV, 230 GeV and 360 GeV.

It can be seen from these figures that only $W^+W^- \rightarrow q_i\bar{q}_j l\nu$ events still affect the stop squark distributions. As $\gamma\gamma \rightarrow W^+W^-$ is a golden channel process at TESLA, it will be relatively easy to remove this background. This is typically done

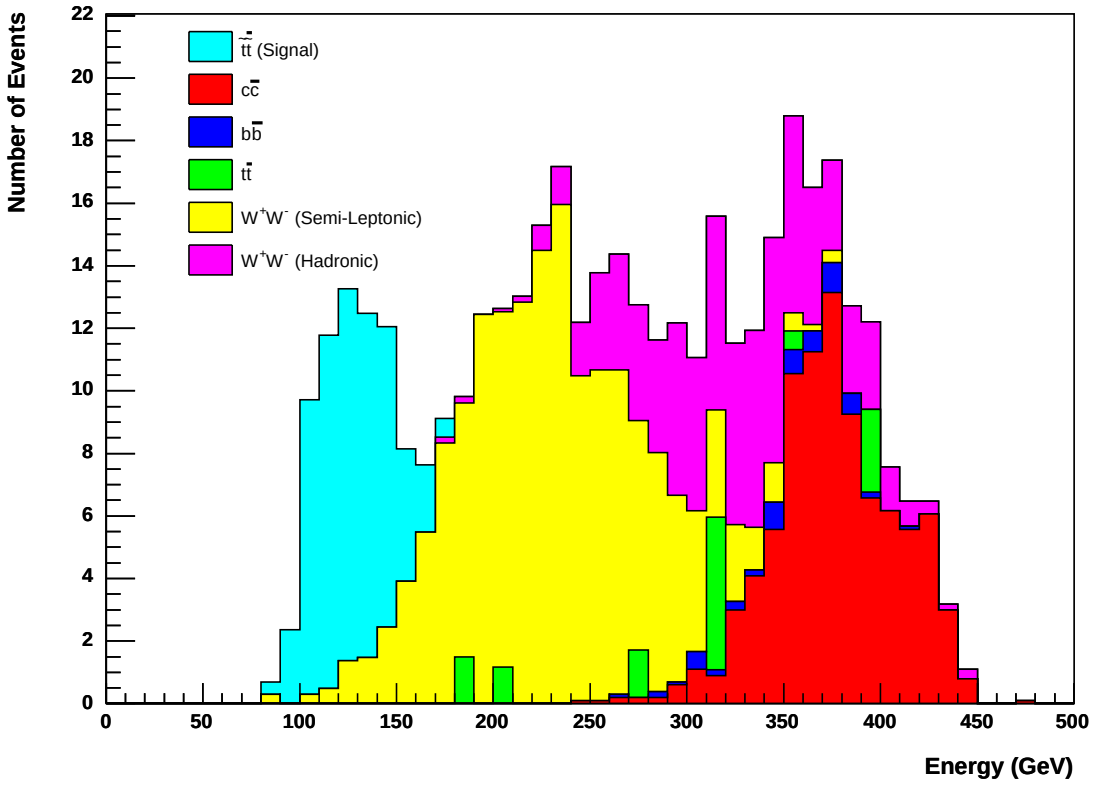

Figure 5.10: Energy Distributions for Signal and Background Events after all cuts have been applied.

by measuring the cross-section for this process, thus determining the number of expected events and their respective distributions after all cuts have been performed.

The number of signal and background events that remain as cuts are performed are given in table 5.4.

Results for a similar analysis performed on single- and double-resolved photon production of $c\bar{c}$ and $b\bar{b}$ pairs are shown in figure 5.11. Applying a thrust angle cut gives background efficiencies of 0.5% and 0.6% for charm-anticharm and beauty-antibeauty events respectively. Due to the forward-peaked nature of these processes, the thrust angle cut is expected to be most effective. After all cuts are performed, surviving events are found to coalesce around the mixed W^+W^- peak. If the generator-level cut on the minimum transverse momentum of charm and beauty jets is assumed to adequately mirror a similar detector-level cut, relatively few events survive. As a result, their contribution to background is negligible.

Cut	Number of Events for $\gamma\gamma \rightarrow$					
	$\tilde{t}\bar{\tilde{t}}$	$c\bar{c}$	$b\bar{b}$	$t\bar{t}$	$q_i\bar{q}_j l\nu$	$q_i\bar{q}_j q_k\bar{q}_l$
No Cut	1,500	293,700	14,300	6,500	702,900	731,500
$-0.7 < \cos\theta_{Thrust} < 0.7$	1,032	31,290	1,959	4,463	202,286	197,388
$p_T > 20\,\text{GeV}$	946	7,798	685	2,449	180,135	18,168
Multiplicity > 25	879	7,777	685	2,447	163,178	18,167
Isolated $e^{\pm}$: $E_T > 20\,\text{GeV}$	851	7,634	670	1,573	105,815	17,345
Isolated $\mu^{\pm}$: $E_T > 20\,\text{GeV}$	824	7,594	664	951	51,174	16,907
Number of Vertices						
Leading Jet = 2	354	3,164	276	258	6,472	2,137
Sub-leading Jet = 2	131	1,168	124	91	637	394
Probability (c not u,d,s)						
Leading Jet > 0.1	87	372	117	89	330	195
Sub-leading Jet > 0.1	69	113	111	84	199	97
Probability (c not b)						
Leading Jet > 0.1	64	100	22	24	170	86
Sub-leading Jet > 0.1	63	89	6	12	166	77

Table 5.4: Number of Simulated Signal and Background Events after cuts are applied. An annual integrated luminosity of 110 fb^{-1} has been assumed.

A similar analysis was carried out on the small sample of light quark events. As expected, the thrust angle and vertex cuts were very effective, yielding background efficiencies of 1% and 6% respectively. After all cuts, around 0.0004% of events remained. These events were concentrated around the hadronic peak, so their contribution to background can be ignored.

5.5.1 Systematic Uncertainties

All data has been taken without consideration of the trigger system that might be in operation at the photon collider. The trigger is responsible for fast data analysis, and chooses events that meet the objectives of the physics program [16]. Depending

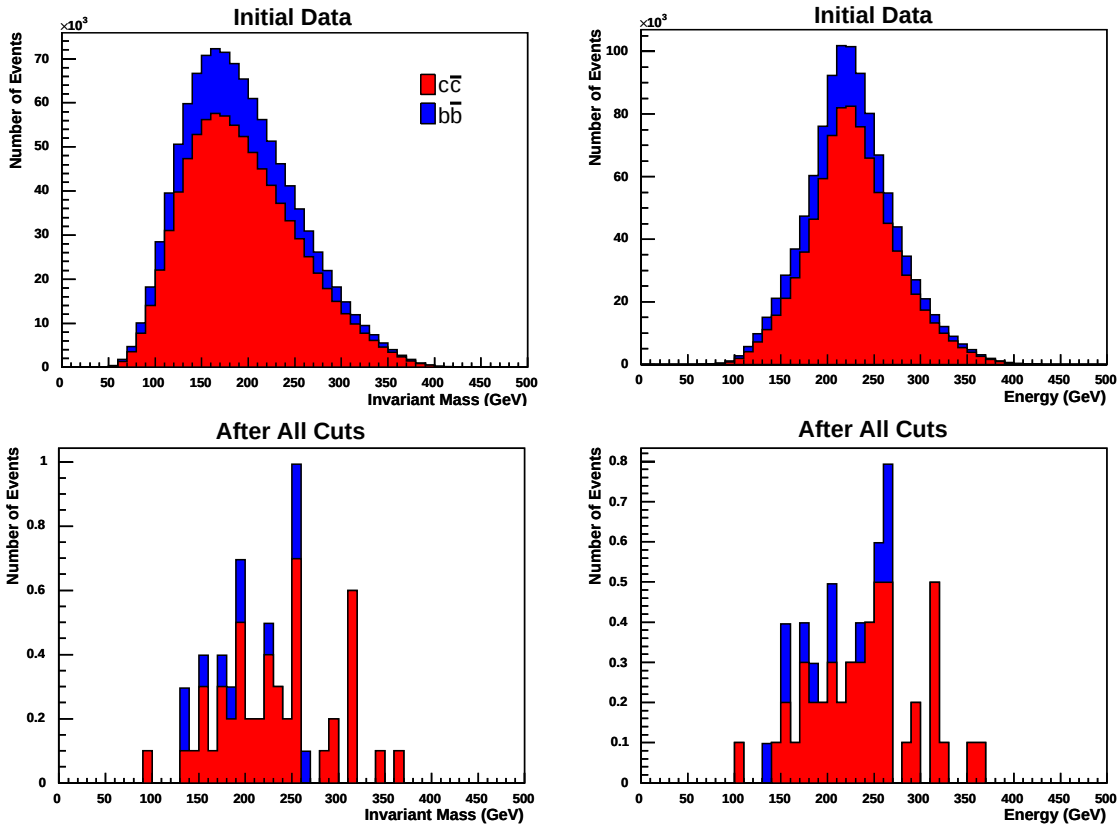

Figure 5.11: Invariant Mass and Energy Distributions for Single- and Double-Resolved $\gamma\gamma \to c\bar{c}$ and $\gamma\gamma \to b\bar{b}$ Events before and after all cuts have been applied

on the efficiency of this system, the number of expected events for each analysed process will vary. Although a triggering system has not been decided on, it could result in an enhancement or reduction of signal and background processes.

There also exists an uncertainty on the efficiency of the cuts that are implemented. Faults with the detector may also interfere with the signal, producing responses for particles that do not exist and giving incorrect properties for those that are found. These effects are not considered by Simdet. The resolution of the detector at the photon collider may be different from that used by Simdet, meaning that there will be some variation in the histograms.

An annual integrated luminosity of $110\,\mathrm{fb}^{-1}$ has been used in this study. Although this is an estimate, the shape of the distributions should not change if this value is incorrect. Additionally, the luminosity is slightly smaller [6] at the lower regions of the high energy peak. This will not affect top and scalar top quark pro-

duction, but will reduce the number of expected events for the other background processes. The photon-energy spectrum determined from the CompAZ routine is a parameterisation, and therefore also has an uncertainty.

5.5.2 Discovery Potential

The significance of the signal gives an indication of the discovery potential of the stop squark. Significance is defined as:

$$\text{Significance} = \frac{N_{signal}}{\sqrt{N_{background}}} \tag{5.4}$$

where N_{signal} and $N_{background}$ are the number of signal and background events respectively. Maximum cuts of 160 GeV were imposed on the invariant mass and energy distributions in an effort to isolate the stop squark peak.

Significances of 10 σ are found from the invariant mass and energy distributions. This shows that there is a very strong potential for stop squark discovery at TESLA. The cross-section for scalar top quark production at a photon collider can be calculated with:

$$\sigma_{\gamma\gamma\to\tilde{t}\tilde{t}} = \frac{N_{events}}{\mathscr{L}\epsilon} \tag{5.5}$$

where N_{events} is the number of events after cuts, $\mathscr{L}$ is the integrated luminosity, and ϵ is the total signal efficiency. A total signal efficiency of 4% is achieved with the cuts employed. The number of stop events that remain are 63 ± 8 (stat), and an annual integrated luminosity of $110\,\text{fb}^{-1}$ is assumed. Systematic errors that contribute to the uncertainty in the luminosity and efficiency are not considered. A result of $13.6 \pm 1.7\,\text{fb}$ is derived, and can be used to determine the stop mass with figure 4.4. A mass fit is not conducted and a value of 180 GeV is assumed for the mass of the stop squark. Michael Klasen's program was used to calculate cross-sections for stop squarks with masses ranging from 170 to 190 GeV, yielding a final value of 180 ± 2 GeV.

Chapter 6

Conclusion

The discovery potential of a scalar top quark of mass 180 GeV has been assessed at the TESLA collider. A 100% branching ratio for the decay chain $\tilde{t}_1 \rightarrow c\tilde{\chi}_1^0$ has been used. The work has been carried out in the context of the Minimal Supersymmetric Standard Model with R-parity conservation, where the neutralino, of mass 100 GeV, is the Lightest Supersymmetric Particle (LSP).

The main background process is $W^+W^- \rightarrow q_i\bar{q}_j l\nu$, which is largely irreducible. Cuts on the thrust angle, transverse momentum, multiplicity, number of vertices and c-jet probabilities have been performed. Additionally, evidence for an isolated lepton has been searched for to remove some main background events.

The invariant mass and energy distributions, after all cuts have been performed, show three peaks corresponding to signal, semi-leptonic and hadronic events in ascending order. For the lowest energy peak, a stop squark signal of significance 10 σ is obtained after all cuts are applied. This indicates that the potential for discovery is very high.

A scalar top pair-production cross-section of 13.6 ± 1.7 fb is determined from a total cut efficiency of 4%, an annual integrated luminosity of 110 fb^{-1} and the number of remaining signal events. Systematic errors on the efficiencies and luminosity have been discussed, but are not included in the final calculation.

A final value of 180 ± 2 GeV was obtained for the mass of the scalar top quark. Although comparable with a value of $180^{+0.69}_{-0.74}$ GeV from a similar analysis [62] per-

formed with electron-positron collisions, photon-photon interactions produce a mass with lower accuracy. This is partly due to a higher number of expected scalar top events in electron-positron interactions, thus giving a lower percentage error. In addition, deducing the mass from the cross-section is heavily dependent on the theory. This leads to unknown theoretical errors. An alternative method was adopted by [62], in which the relationship between the mass of the scalar top quark and the stop mixing angle was determined with polarised electrons and positrons. The use of this technique, with polarised photon collisions, should greatly improve the accuracy of the determined mass. However, this approach still relies on the theory.

Other possiblities for measuring the mass of the scalar top quark from the final state have been investigated in the case of electron-positron collisions [63]. Jet energy spectrum endpoint measurements contain information concerning the masses of both the charm quark and the neutralino, which will not be seen in this case. The minimum mass method [64] requires the mass of the neutralino to be known, thus allowing the calculation of the minimum allowed mass of both charm jets. Although these techniques lead to larger errors [63], they are independent of the theory.

To optimise the selection efficiency, an Iterative Discriminant Analysis (IDA) [65] can be implemented. This method was used in [62], and could be used to reduce the magnitude of errors on the stop squark mass.

Only one set of values for the stop squark and neutralino masses have been considered. A more thorough investigation could scan the entire mass range for these particles.

Additionally, particle pair-production in electron-photon interactions has not been considered. The high-energy luminosity of these collisions at the TESLA photon collider is 94 fb^{-1} [6], indicating that this could affect the distributions presented here. A complete analysis should consider these processes.

The production of the Higgs boson and other supersymmetric particles has not been considered. These processes could be another source of background. Although the masses of these un-detected particles are still not known, further analysis could be performed over their kinematically allowed mass range.

Appendix A

Determination of Momentum-Energy Vectors

Signal and top quark background events, after extraction from the Monte Carlo generator, were expressed in terms of their transverse momentum and the rapidities of both particles. The spherical coordinate system for the momentum of these particles is illustrated in figure A.1, where the origin is located at the interaction point.

The magntiude of a particle's momentum component in the xy-plane is called the transverse momentum, and can be expressed by:

$$p_T = \sqrt{p_x^2 + p_y^2} \tag{A.1}$$

where p_x and p_y are respectively the x- and y-components of the particle's momentum. From figure A.1, the azimuthal angle is defined as $\tan\phi = \frac{p_y}{p_x}$. By writing equation A.1 in terms of p_x, the expression for the azimuthal angle becomes $\tan\phi = \frac{p_y}{\sqrt{p_T^2 - p_y^2}}$. This leads to the following equation for p_y:

$$p_y = p_T \sin\phi \tag{A.2}$$

A random number generator is used to assign a value between 0 and 2π radians for the azimuthal angle. As both signal and top quark background generation result in a two-body process, the particles are created in opposite directions to each other

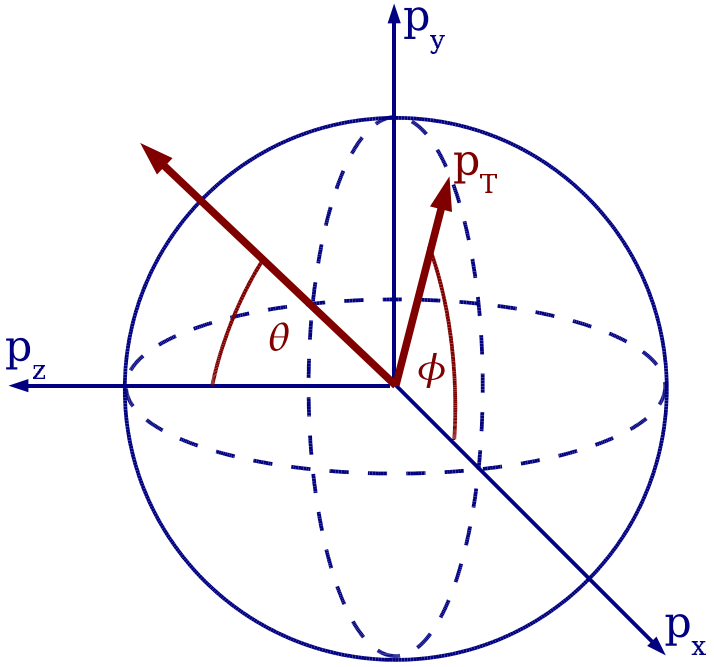

Figure A.1: Spherical Coordinate System at TESLA in terms of Momentum Vectors. The polar angle θ lies in the yz-plane.

in the xy-plane to conserve momentum. Therefore, the momentum of the second particle in the y-direction is given the opposite value. These values for p_y are used to calculate the momentum in the x-direction:

$$p_x = \sqrt{p_T^2 - p_y^2} \tag{A.3}$$

Rapidity is a dimensionless variable used to describe the behaviour of a particle. It is defined as:

$$y = \frac{1}{2} \log \frac{E + p_z}{E - p_z} \tag{A.4}$$

where E is the energy and p_z is the momentum in the z-direction. Equation A.4 corresponds to $\tanh(y) = \frac{p_z}{E}$. The energy of a particle is $E = \sqrt{p_T^2 + p_z^2 + m^2}$, where m is its mass. Therefore, the rapidities of both particles $y_{1,2}$ can be used to determine their z-momentum components and energies:

$$p_{z_{1,2}} = \sinh(y_{1,2}) \sqrt{p_T^2 + m^2} \qquad E_{1,2} = \frac{p_{z_{1,2}}}{\tanh(y_{1,2})} \tag{A.5}$$

References

[1] TESLA Collaboration, *"TESLA: The Superconducting Electron-Positron Linear Collider with an Integrated X-Ray Laser Laboratory: Technical Design Report, Volumes 1-6"*, DESY 2001-011, ECFA 2001-209, TESLA Report 2001-23, TESLA-FEL 2001-05

[2] NLC Collaboration, *"2001 Report on the Next Linear Collider: A Report Submitted to Snowmass 2001"*, FERMILAB-Conf-01/075-E, LBNL-PUB-47935, SLAC-R-571, UCRL-ID-144077

[3] GLC Collaboration, *"GLC Project: Linear Collider for TeV Physics"*, KEK-Report-2003-7

[4] Battaglia, A., De Roeck, A., Ellis, J. & Schulte, D., *"Physics at the CLIC Multi-TeV Linear Collider: Report of the CLIC Physics Working Group"*, CERN-2004-005

[5] Augustin, J-E, *et al.*, International Technology Recommendation Panel, *"Executive Summary"*, http://www.interactions.org/pdf/ITRPexec.pdf, August 2004

[6] Badelek, B. *et al.*, ECFA/DESY Photon Collider Working Group Collaboration, *"TESLA Technical Design Report, Part VI, Chapter 1: Photon Collider at TESLA"*, hep-ex/0108012, August 2001

[7] Noble, R.J., Nucl. Instrum. Methods Phys. Res. A **256**, 427 (1987)

[8] Telnov, V., Nucl. Instrum. Methods Phys. Res. A **494**, 35 (2002)

[9] Ginzburg, I.F., Kotkin, G.L., Serbo, V.G. & Telnov, V.I., Nucl. Instrum. Methods Phys. Res. **205**, 47 (1983)

[10] Telnov, V.I., Nucl. Instrum. Methods Phys. Res. A **294**, 72 (1990)

[11] Xie, M., Kim, K.-J. & Sessler, A., Nucl. Instrum. Methods Phys. Res. A **355**, 163 (1995)

[12] Kotkin, G.L., Serbo, V.G. & Telnov, V.I., Phys. Rev. ST Accel. Beams **6**, 011001 (2003)

[13] Sjöstrand, T., Lönnblad, L. & Mrenna, S., *"PYTHIA 6.2 Physics and Manual"*, hep-ph/0108264, August 2001
Sjöstrand, T. *et al.*, Comput. Phys. Commun. **135**, 238 (2001)

[14] Żarnecki, A.F., Acta Phys. Polon. B **34**, 2741 (2003)

[15] Alexander, G. *et al.*, *"TESLA Technical Design Report, Part IV: A Detector for TESLA"*, DESY-2001-011, ECFA-2001-209, TESLA Report 2001-23, TESLA-FEL 2001-05

[16] Aguilar-Saavedra, J.A. *et al.*, ECFA/DESY LC Physics Working Group Collaboration, *"TESLA Technical Design Report, Part III: Physics at an e^+e^- Linear Collider"*, hep-ph/0106315, June 2001

[17] Martin, B.R. & Shaw, G., *"Particle Physics: Second Edition"*, John Wiley & Sons (1997)

[18] Eidelman, S. *et al.*, Particle Data Group Collaboration, *"Review of Particle Physics"*, Phys. Lett. B **592**, 1 (2004)

[19] Halzen, F. & Martin, A.D., *"Quarks & Leptons: An Introductory Course in Modern Particle Physics"*, John Wiley & Sons (1984)
Rosner, J.L., *"The Standard Model in 2001"*, hep-ph/0108195, May 2002

[20] Smy, M.B. *et al.*, Super-Kamiokande Collaboration, Phys. Rev. D **69**, 011104 (2004)

[21] Sakharov, A.D., Pisma Zh. Eksp. Teor. Fiz. **5**, 32 (1967), [JETP Lett. **5**, 24 (1967)]

[22] Polonsky, N., *"Supersymmetry Structure and Phenomena"*, hep-ph/0108236, August 2001

[23] Olive, K.A., *"Introduction to Supersymmetry: Astrophysical and Phenomenological Constraints"*, hep-ph/9911307, November 1999

[24] Kane, G., *"Supersymmetry: Squarks, Photinos, and the Unveiling of the Ultimate Laws of Nature"*, Perseus Publishing (2000)

[25] Haag, R., Lopuszànski, J.T. & Sohnius, M., Nucl. Phys. B **88**, 257 (1975)

[26] Farrar, G.R. & Fayet, P., Phys. Lett. B **76**, 575 (1978)

[27] Barbier, R. *et al.*, *"R-parity Violating Supersymmetry"*, hep-ph/0406039, June 2004

[28] Ellis, J., *"Supersymmetry for Alp Hikers"*, hep-ph/0203114, March 2002

[29] Haber, H.E., Nucl. Phys. Proc. Suppl. **62**, 469 (1998)

[30] Miller, D.J., Nevzorov, R. & Zerwas, P.M., Nucl. Phys. B **681**, 3 (2004)

[31] Hall, L.J. & Suzuki, M., Nucl. Phys. B **231**, 419 (1984)

[32] Dimopoulos, S. & Georgi, H., Nucl. Phys. B **193**, 150 (1981)

[33] Roy, P., Pramana **60**, 169 (2003)

[34] Hall, L., Lykken, J. & Weinberg, S., Phys. Rev. D **27**, 2359 (1983)

[35] de Wit, B., *"Supergravity"*, hep-th/0212245, December 2002

[36] Dine, M. & Nelson, A.E., Phys. Rev. D **48**, 1277 (1993)

[37] Heister, A. *et al.*, ALEPH Collaboration, Eur. Phys. J. C **24**, 177 (2002)
Abbiendi, G. *et al.*, OPAL Collaboration, Phys. Lett. B **546**, 29 (2002)

[38] Georgi, G. & Glashow, S.L., Phys. Rev. Lett. **32**, 438 (1974)

[39] Dermišek, R., Mafi, A. & Raby, S., Phys. Rev. D **63**, 035001 (2001)

[40] Espinosa, J.R., Quirós, M. & Zwirner, F., Phys. Lett. B **307**, 106 (1993)

[41] Bartl, A. *et al.*, Z. Phys. C **76**, 549 (1997)

[42] Porod, W. & Wöhrmann, T., Phys. Rev. D **55**, 2907 (1997)
Djouadi, A. & Mambrini, Y., Phys. Rev. D **63**, 115005 (2001)

[43] Hikasa, K-I. & Kobayashi, M., Phys. Rev. D **36**, 724 (1987)

[44] Beenakker, W., Höpker, R., Plehn, T. & Zerwas, P.M., Z. Phys. C **75**, 349 (1997)

[45] Choi, S.Y., Kalinowski, J., Moortgat-Pick, G. & Zerwas, P.M., Eur. Phys. J. C **22**, 563 (2001)

[46] Bottino, A. *et al.*, Nucl. Phys. Proc. Suppl. **31**, 359 (1993)

[47] Bauer, T.H., Spital, R.D., Yennie, D.R. & Pipkin, F.M., Rev. Mod. Phys. **50**, 261 (1978)

[48] Tîmneanu, N., Kwieciński, J. & Motyka, L., Eur. Phys. J. C **23**, 513 (2002)

[49] Berge, S., Klasen, M. & Umeda, Y., Phys. Rev. D **63**, 035003 (2001)
Klasen, M., Nucl. Instrum. Methods Phys. Res. A **472**, 160 (2001)

[50] Ginzburg, I.F. *et al.*, Nucl. Instrum. Methods Phys. Res. **219**, 5 (1984)

[51] Klasen, M., Private Communication

[52] Telnov, V., Nucl. Instrum. Methods Phys. Res. A **355**, 3 (1995)

[53] Schuler, G.A. & Sjöstrand, T., Nucl. Phys. B **407**, 539 (1993)
Friberg, C. & Sjöstrand, T., Phys. Lett. B **492**, 123 (2000)

[54] Jikia, G., Nucl. Phys. B **405**, 24 (1993)

[55] Andersson, G., Gustafson, G., Ingelman. G. & Sjöstrand, T., Phys. Rept. **97**, 31 (1983)
Sjöstrand, T., Nucl. Phys. B **248**, 469 (1984)

[56] Norrbin, E. & Sjöstrand, T., Eur. Phys. J. C **17**, 137 (2000)

[57] Pohl, M. & Schrieber, H.J., *"SIMDET - Version 4: A Parametric Monte Carlo for a TESLA Detector"*, hep-ex/0206009, June 2002

[58] Behnke, T. & Blair, G.A., *"BRAHMS - Version 102: A Monte Carlo for a Detector at a 500-GeV to 800 GeV Linear Collider"*, LC-PHSM-2001-005

[59] Jackson, D.J., Nucl. Instrum. Methods Phys. Res. A **388**, 247 (1997)

[60] Kuhl, T., Nucl. Instrum. Methods Phys. Res. A **511**, 221 (2003)

[61] Kuhl, T., Private Communication

[62] Finch, A., Nowak, H. & Sopczak, A., *"A Scalar Top Study with c-Quark Tagging at a Linear e^+e^- Collider"*, EPS-paper 370, July 2003

[63] Finch, A., Sopczak, A. & Nowak, H., *"Determination of the Scalar Top Mass at a Linear e^+e^- Collider"*, to be published in Proceedings of the LCWS (Linear Collider Workshop) 2004

[64] Feng, J.L. & Finnell, D.E., Phys. Rev. D **49**, 2369 (1994)

[65] Malmgren, J. & Johansson, K., Nucl. Instrum. Methods Phys. Res. A **403**, 481 (1998)